

## Measurement of diffuse and plane of array irradiance by a combination of a pyranometer and an all-sky imager

Niklas Benedikt Blum<sup>a,b,\*</sup>, Stefan Wilbert<sup>a</sup>, Bijan Nouri<sup>a</sup>, Jorge Lezaca<sup>b</sup>, David Huckebrink<sup>a</sup>, Andreas Kazantzidis<sup>c</sup>, Detlev Heinemann<sup>b</sup>, Luis F. Zarzalejo<sup>d</sup>, María José Jiménez<sup>e</sup>, Robert Pitz-Paal<sup>f</sup>

<sup>a</sup> Deutsches Zentrum für Luft- und Raumfahrt (DLR), Institut für Solarforschung, Paseo de Almería, 73, 2, E-04001 Almería, Spain

<sup>b</sup> DLR, Institut für Vernetzte Energiesysteme, Carl-von-Ossietzky-Straße 15, 26129 Oldenburg, Germany

<sup>c</sup> Laboratory of Atmospheric Physics, Department of Physics, University of Patras, 26500 Patras, Greece

<sup>d</sup> CIEMAT Energy Department – Renewable Energy Division, Avda. Complutense, 40, 28040 Madrid, Spain

<sup>e</sup> CIEMAT Energy Department – Renewable Energy Division, Energy Efficiency in Buildings R & D Unit, Avda. Complutense, 40, 28040 Madrid, Spain

<sup>f</sup> DLR, Institut für Solarforschung, Linder Höhe, 51147 Köln, Germany

### ARTICLE INFO

#### Keywords:

Shortwave radiation  
All-sky imager  
Global tilted irradiance (GTI)  
Plane of array irradiance (POA)  
Transposition  
Sky radiance

### ABSTRACT

Accurate, robust and cost-efficient measurements of diffuse horizontal irradiance (DHI) and global tilted irradiance (GTI) are of great interest for solar energy applications. However, the available measurement techniques exhibit at least one of these shortcomings: restriction of GTI measurement to a single plane, intensive maintenance, high acquisition cost or increased deviations, especially at new measurement sites. To avoid these shortcomings, we suggest a comparably inexpensive and robust setup of a thermopile pyranometer and an all-sky imager (ASI) for measurement of DHI and GTI. The pyranometer measures global horizontal irradiance (GHI) and our method consecutively estimates diffuse sky radiance, DHI, direct normal irradiance (DNI) and GTI, by merging information from the combined setup. The system is developed and validated at two sites in Spain and Germany. Measurement of GTI is benchmarked for seven planes over GTI derived by transposition based on DHI and DNI from a tracker setup with a pyrhelimeter and shaded thermopile pyranometer. Our results indicate that the measurement system can be applied at both sites. The proposed method avoids time-consuming radiometric calibrations of the camera by the combination of both sensors and a self-calibration. The measurement system is promising in particular for measurement of GTI. For 10-min average GTI, our approach yields an rRMSD of 1.6...4.8% for planes with tilts in the range of 20°...61°. Thus, at both sites and for all planes, it outperforms the tracker-based transposition yielding 2.3...6.5%. DHI is measured significantly more accurately than reported in previous works using an ASI alone.

### 1. Introduction

Accurate measurements of global tilted irradiance (GTI) are crucial for solar energy applications. GTI is required to predict the output of a photovoltaic (PV) generation or non-concentrating solar thermal collectors. Therefore, knowledge of GTI is important for tasks like resource assessment in the planning process of a PV installation, monitoring a PV plant and quickly identifying abnormalities, as well as to optimize the operation of PV plants. For the latter task, forecasting systems relying on measurements of solar irradiance and one or multiple all-sky imagers (ASIs), e.g. fisheye cameras with 180° field of view used to observe the whole sky, have been demonstrated (Nouri et al., 2020; West et al., 2014).

Besides these applications, GTI is essential to compute the overall radiant power received by the surface of a building. Such knowledge then allows to model a building's thermal characteristics (Kim et al., 2016; Li and Lam, 2004; Loutzenhiser et al., 2007) and to control the climatization of a building (Clarke et al., 2002; Lazos et al., 2014), for example. Further, it may be advantageous to assess and monitor GTI received by *building-integrated photovoltaics* (BIPV) to optimize the energy management of buildings (Toledo et al., 2020).

For concentrating solar technologies, direct normal irradiance (DNI) is required. DNI can be derived from diffuse horizontal irradiance (DHI) and GHI.

\* Corresponding author at: DLR, Institut für Vernetzte Energiesysteme, Carl-von-Ossietzky-Straße 15, 26129 Oldenburg, Germany.  
E-mail address: [niklas.blum@dlr.de](mailto:niklas.blum@dlr.de) (N.B. Blum).

<https://doi.org/10.1016/j.solener.2021.11.064>

Received 16 June 2021; Received in revised form 17 November 2021; Accepted 24 November 2021

Available online 7 January 2022

0038-092X/© 2021 The Author(s). Published by Elsevier Ltd on behalf of International Solar Energy Society. This is an open access article under the CC BY

license (<http://creativecommons.org/licenses/by/4.0/>).

Measurement equipment known so far for the measurement of GTI and its composition or of DNI is costly and/or limited in its scope. GTI in a single plane is measured with relatively high accuracy and at a high temporal resolution by a pyranometer in the respective plane. However, this measurement principle does not provide information on the angular composition of GTI. In PV power plants this angular composition is of interest to better understand and model the performance as the incidence angle affects the module performance (Elminir et al., 2001; Mungra et al., 2021). For tracked or bifacial PV the angular composition is of even higher interest. Also using one tilted pyranometer, only one specific GTI or plane of array (POA) is assessed and the determination of the ideal tilt angle based on such measurements would require several pyranometers. The calculation of GTI in arbitrary planes via transposition models based on DNI and DHI, received from a solar tracker, induces significant inaccuracies. For a temporal resolution of 1 min, rRMSD in the range of 6 and 10% for planes with a tilt of 45° and 90° are observed frequently (Demain et al., 2013; Gueymard, 2009; Yang, 2016). Additionally, Solar trackers are delicate, as they have to follow the sun accurately to measure DHI with a shaded thermopile pyranometer and DNI with a pyrliometer. Also, pyrliometers are much more affected by soiling than other radiometers (Geuder and Quaschnig, 2006). Consequently, the setup comes at considerable costs and requires frequent checks and maintenance (Sengupta et al., 2017). In solar energy applications, alternative, more economical solutions are therefore required which either avoid a solar tracker to measure DNI and DHI or provide GTI in arbitrary planes directly.

Besides solar trackers, there are more economical approaches to retrieve DNI and DHI which in general yield larger uncertainties. These radiometer systems include *rotating shadowband irradiometers* (RSI, Wilbert et al., 2016) and multi sensor instruments using either different measurement planes (Sunto CaptPro sensor, sunto, 2018) or shading masks (Delta-T SPN1, Vuilleumier et al., 2017). Vuilleumier et al. (2017) found RMSDs of around 10 W/m<sup>2</sup> when measuring DHI by different RSI models and an RMSD of around 20 W/m<sup>2</sup> when measuring DHI by SPN1. Additionally the SPN1 exhibited a significant BIAS of around -10 W/m<sup>2</sup>. In our own tests, Sunto CaptPro exhibited deviations which were not acceptable. As most basic option involving only a single horizontally aligned pyranometer, DNI and DHI can be estimated roughly from global horizontal irradiance (GHI) or GTI by decomposition models. Lave et al. (2015) benchmarked several decomposition models at five sites. For the most accurate model (DIRINT), an RMSD in the range of 8...14% relative to the present GHI was attested, evaluating hourly averages of DHI. Ineichen (2008) found an rRMSD of around 23% for DIRINT and other decomposition models when estimating hourly averaged DNI. Additionally, these approaches and also the transposition models perform very differently depending on the meteorological conditions on site (Gueymard, 2009; Vuilleumier et al., 2017). Therefore, alternative solutions are of interest.

To assess GTI and its angular composition in an arbitrary plane rigorously, sky radiance must be measured. Specialized equipment has been developed for this task such as a multidirectional spectroradiometer (Riechelmann et al., 2013) or sky scanners, described by Ineichen (2007). These measurements of sky radiance have been used to develop transposition models (Li and Lam, 2004), for reconstruction of atmospheric properties (Dubovik and King, 2000) or validation of daylighting simulations (Reinhart and Walkenhorst, 2001). However, these instruments are rather used in laboratory setups and not for measurement of GTI in real time and in the field. Sky scanners exhibit a comparably low temporal resolution and inaccurate radiance measurements at sun distance angles below 15...20° (Gueymard and Ivanova, 2018). Some ASIs have been developed specifically to measure sky radiance or luminance. ASIs of this type are typically calibrated radiometrically (e.g. Mejia et al., 2016; Tohsing et al., 2013) and were often equipped with shading devices (Dev et al., 2014; Román et al., 2012; Rossini and Krenzinger, 2007; Shields et al., 1998; Voss and Zibordi, 1989). Some authors apply ASIs only to specific sky conditions

such as overcast (Lee and Devan, 2008). These specialized ASI setups may introduce increased acquisition cost and maintenance and are only in part suitable for an operation in the field.

More common fisheye cameras are used as ASIs to forecast solar irradiance and PV production for the immediate future of typically up to 20 min ahead. This type of forecasting is referred to as nowcasting in the following. Authors from the field of ASI-based nowcasting of solar irradiance tested fisheye cameras to estimate irradiance in order to reduce system costs by avoiding radiometers. There, focus was on measurements of GHI, DNI, DHI based on the camera alone rather than GTI from the combination of ASI and pyranometer. Alonso-Montesinos and Batlles (2015) used a camera similar to the ones used here. These authors equipped the ASI with a shadow band and applied a statistical approach to estimate DNI, DHI, GHI. Dev et al. (2019) estimated GHI by a statistical method based on luminance calculated for 5000 pixels distributed over the ASI image. Schmidt et al. (2015) predicted DNI and DHI from ASI images by a k nearest neighbor (kNN) model which predicted the respective clear sky index as an intermediate step. This model outperformed satellite-based estimation of hourly GHI. Siddiqui et al. (2019) estimated GHI from ASI image by a convolutional neural network. Gauchet et al. (2012) segmented the ASI image into five classes of sky and cloud. Consecutively, they applied linear regression to estimate DNI, DHI and GHI, effectively determining average values for the ratio of radiance over clear sky irradiance per class. Kurtz and Kleissl (2017) tested a camera developed specifically to be applied as ASI to measure DNI, DHI and GHI. The authors applied a physics based camera model and post-processed the measurements by a neural network. These prior studies in general attested significant deviations of the measured irradiance components with an RMSD ranging around 60...80 W/m<sup>2</sup> for GHI, 120...190 W/m<sup>2</sup> for DNI, 70...80 W/m<sup>2</sup> for DHI. These deviations were reported for validations at the site of model development using different temporal resolutions. A part of these studies only provided validations for certain cloud conditions and only for limited measurement periods.

Authors that used more physical models (Chauvin et al., 2015; Kurtz and Kleissl, 2017) attested that direct and circumsolar irradiance can impact the ASI image especially near the sun's position via glare and saturation. Furthermore, the camera firmware's exposure control affected the measurement as it equalized image properties under certain sky conditions (Chauvin et al., 2015).

To overcome these challenges, we propose to modify the measurement setup and to evaluate the ASI image together with the reading of a thermopile pyranometer, online. This combination and the inclusion of commonly available image meta data allows to check, correct and self-calibrate major influences present in the measurement. Validity of the approach is assured by tests at two distinct sites. Compared to previous studies, an emphasis here is made on the measurement of GTI for arbitrary planes. In particular, the method aims to be more accurate than conventional approaches to estimate GTI. At the same time, by employing a regular fisheye surveillance camera and an ISO 9060:2018 Class A thermopile pyranometer, it uses economical, robust and low-maintenance hardware without moving parts. This setup fulfills the requirements for highest accuracy, which are set by relevant IEC and ISO standards (e.g. International Electrotechnical Commission, 2015; International Organization for Standardization, 2018). Especially, the inclusion of a spectrally flat radiometer is expected to bring a general advantage of the method, compared to approaches relying on an ASI alone. The used setup can also provide DHI and therefore DNI for concentrating solar technologies and has the potential for further functionalities of sky condition monitoring in the future. To the best of our knowledge, such a combined evaluation method has not been studied in the literature yet for measurement of DHI and GTI.

This publication is structured as follows. First, the used experimental setups at two separate sites are introduced in Section 2. Next, in Section 3, the measurement procedure is presented: Section 3.1 details how sky radiance is measured from RGB images. Consecutively,

Section 3.2 explains how irradiance components of interest are received from sky radiance and the pyranometer reading. Corrections to this measurement, which employ information available in the combined setup, are studied in Section 3.3. The DHI measurement is validated in Section 4.1. Section 4.2 presents the GTI validation and benchmarks the system against conventional approaches to estimate GTI by transposition. Finally, Section 5 recapitulates the study.

## 2. Experimental setup

This study uses datasets from two sites in Europe. CIEMAT's Plataforma Solar de Almería (PSA, see Fig. 1, top) in southern Spain is used to develop the model. PSA and University of Oldenburg (UOL, see Fig. 1, bottom), located in northwest Germany, are used for the validation. Each setup features an all-sky imager (ASI), measuring in particular DHI and diffuse sky irradiance in tilted planes ( $D_t$ ), a pyranometer to measure GHI, a shaded pyranometer to develop and validate the DHI measurement, a pyrheliometer, providing DNI, and various tilted pyranometers to validate and benchmark the measurement of GTI. ASI and irradiance measurements are located at a distance of less than 20 m at both sites. Relevant information on the measurements at both sites is compiled in Table 1. The study only uses ISO 9060:2018 Class A thermopile pyranometers. All instruments used at PSA are calibrated biannually according to international standards (International Organization for Standardization, 1993). For all pyranometers, which are used at PSA to measure global tilted and horizontal irradiance, this calibration is overridden by a calibration relative to the reference GHI used in this study, i.e. relative to GHI calculated from DNI and DHI measured by pyrheliometer and shaded pyranometer of the solar tracker. At site UOL, the instruments were calibrated less than three years before end of the presented measurement campaign. Both sites are equipped with measurements of dry-bulb temperature and humidity.

The ASIs used here are Mobotix fisheye surveillance cameras (specifications see Table 1), which have been used in prior studies for ASI-based nowcasting (Alonso-Montesinos and Battles, 2015; Nouri et al., 2020; West et al., 2014) and sky condition monitoring (Kazantzidis et al., 2017; Wacker et al., 2015). As the studied ASIs are intended for nowcasting, they were already calibrated geometrically in the past. The intrinsic calibration used is described by Scaramuzza et al. (2006). Additionally, at each site the moon was captured during multiple nights in which the illumination of the moon would under clear conditions have been at least 90% of the value at full moon. Consecutively, the camera orientation was adapted to minimize the deviation (RMSD in pixels) of astronomically expected and actually found position of the moon in each image.

ASI images are taken every full and half minute and evaluated at the same rate. Irradiance and meteorological measurements are acquired at 1 s resolution. All analyzed quantities, especially irradiance measured and calculated based on the ASI images, are transformed to 1 min averages before any further processing.

The sensors are cleaned on weekdays at PSA and weekly at UOL. The reference measurements at PSA were quality controlled each weekday with a method described in Geuder et al. (2015). Automatic filters using the three component test and other filters were applied to guide the expert during the inspection. For UOL, these quality checks were applied retrospectively, after the measurement period. The GTI measurements were also inspected visually. Further, the measurements were compared to nearby stations at distances smaller than 1 km, at both sites. This study followed the recommendation stated in Vuilleumier et al. (2017): Measurements taken at a sun elevation of less than 10° were rejected, to avoid inconsistencies between measurements due to obstacles shading some of the sensors.

Studied sites feature distinct meteorological and surrounding conditions. According to Kottek et al. (2006), PSA exhibits a cold-arid steppe climate (BSk), whereas UOL is characterized as temperate oceanic

**Table 1**

Measurement equipment, measured quantities and datasets used at the sites University of Oldenburg (UOL) and CIEMAT's Plataforma Solar de Almería (PSA). For GTI measurements tilt angle ( $\delta$ ) and azimuth angle over north ( $\phi$ ) are provided.

Equipment or site property	Measured quantity	CIEMAT's plataforma Solar de Almería (PSA)	University of Oldenburg (UOL)
Latitude, Longitude, Altitude [ $^{\circ}$ N, $^{\circ}$ E, m]		37.091, -2.358, 496	53.152, 8.166, 20
Period development		01.07.–31.12.2019	
Period validation		01.01.–16.06.2020	12.04.–07.10.2019
ASI Model	DHI, $D_t$	Q26B-6D	Q25
Resolution (effective)		6MP (4MP)	6MP (4MP)
Color temperature		10 000 K	5500 K
Firmware		MX-V5.2.1.4	MX-V4.4.2.73
Pyrheliometer	DNI	CHP1	CHP1
Shaded pyranometer	DHI	CMP21, ventilated, heated, shaded by shading ball	CM11, ventilated, heated, shaded by shading ball
Pyranometer	GHI	CMP21 ventilated, heated, on fixed table	CM11 ventilated, heated, on fixed table
Pyranometer	GTI ( $\delta, \phi$ )	CMP21 (45°, 225°)	CM11 (45°, 225°)
Pyranometer	GTI ( $\delta, \phi$ )	CM11 (20°, 180°)	CM11 (45°, 135°)
Pyranometer	GTI ( $\delta, \phi$ )	CMP21 (30°, 180°)	CM11 (45°, 180°)
Pyranometer	GTI ( $\delta, \phi$ )	–	CM11 (61°, 184.2°)
Solar tracker		EKO STR-22G with sun sensor	Sci-Tec Instruments 2AP with sun sensor

(Cfb). The PSA setup is located in a semi-desert featuring sparse grass, bushes, mostly dry soil and gravel (see Fig. 1, top). All sensors are placed 0.8...1.5 m over ground. The UOL setup is located on the highest rooftop of a building surrounded by green area with various deciduous trees (see Fig. 1, bottom). The near field at UOL consists of concrete and brick surfaces. These surroundings affect albedo at the site. We weight tabulated spectral reflectance for various surface types from SMARTS 2.9.5 (Gueymard, 2001, 2005) by a standard irradiance spectrum and average over the latter to yield albedo of a surface type. Then, albedo values of the surface types present at the site are averaged. As reference spectrum of solar irradiance, hemispherical tilted irradiance given by ASTM G173-03 (ASTM, 2020) at air mass 1.5 is used. With the surface types listed above, albedo values of 0.23 and 0.3 are determined for PSA and UOL, respectively.

## 3. Measurement of sky radiance, diffuse sky irradiance, DNI and GTI based on ASI and pyranometer

This section describes the proposed method to measure GHI, DHI, DNI and finally GTI in the combined setup of ASI and pyranometer. The measurement procedure utilizes consecutive steps which are explained in the following subsections. First, sky radiance is calculated from the ASI image based on a camera model (Section 3.1). Thereafter, sky radiance and GHI measured by the pyranometer are combined to yield all irradiance components of interest (Section 3.2). The latter step is supported by a number of corrections relying on GHI and information on the image processing of the ASI. In Section 3.3, these corrections are parameterized and the self-calibration of ASI-based DHI to pyranometer-based GHI is introduced, which relies on conditions with negligible direct irradiance.

### 3.1. Estimation of radiance from ASI RGB images

This section describes a procedure to estimate sky radiance based on an RGB image captured by an ASI. First, a camera response model provides the relationship of spectral irradiance incident on a pixel and the intensity in the ASI image. Estimations of the spectral distribution of daylight then allow to estimate pixelwise broadband irradiance. Finally, through knowledge of the camera's optics, sky areas and pixels are related and thus sky radiance is approximated.



Fig. 1. Setup at CIEMAT's PSA (top row): Solar tracker with pyrheliometer and shaded pyranometer (left), pyranometers in 3 tilted planes (center) and ASI (right). The pyranometer providing GHI for the combination is not depicted. Setup at UOL (bottom row): pyranometers in 4 tilted planes (left, center) and ASI with ventilation and heating unit (right) and additional ASI (center, not used here). The solar tracker providing DHI, DNI, GHI is not depicted. For details on the sites see also Table 1. (For interpretation of the references to color in this figure legend, the reader is referred to the web version of this article.)

A camera response model relates spectral irradiance  $E_{mn,\lambda}$  incident on pixel  $mn$  of the chip and the intensities  $S_{mn}$  in the color channels R, G, B of pixel  $mn$  in the camera image. The radiometric camera model

$$S_{mn} = \Gamma \left( \mathbf{M} \Delta t \int_{A_{mn}} \int_{\Lambda_{sensitive}} \epsilon_{mn}(\lambda) E_{mn,\lambda}(\lambda) d\lambda dA + \underline{n} \right) \quad (1)$$

corresponds with the one used by Kuhn et al. (2017).  $\Gamma$  indicates the non-linear Gamma-correction, applied to each channel (R, G, B) independently.  $\mathbf{M}$  is the constant mixing matrix, a full matrix of size  $3 \times 3$ .  $\epsilon_{mn}$  are the camera's spectral sensitivities per color channel.  $A_{mn}$  is the surface covered by pixel  $mn$ .  $\Lambda_{sensitive}$  is the interval of wavelengths in which the camera responds to spectral irradiance.  $\underline{n}$  represents the dark signal.

Eq. (1) is inspected and customized for the used type of fish-eye camera. Gamma correction  $\Gamma$  was determined by the procedure of Grossberg and Nayar (2002) comparing images captured at varied exposure time. Based on this, it is reverted to yield intensities of the linearized RGB-image  $S'_{mn} = \Gamma^{-1}(S_{mn})$ . The dark signal  $\underline{n}$  is expected to cause a positive offset of received image intensity. Exposures from dark conditions suggested that  $\underline{n}$  is negligible for the used acquisition settings. Exposure time  $\Delta t$  is kept constant over time by the used camera settings.

The camera's spectral sensitivities  $\epsilon_{mn}$  are proportional to the camera chip's quantum efficiencies over wavelength  $\lambda$ . The constant mixing matrix  $\mathbf{M}$  is applied by the camera firmware. It corrects for deviations between the camera chip's actual spectral sensitivities  $\epsilon_{mn}$  per channel and the spectral responses  $\epsilon_{s,mn}$  defined by the color space of the delivered image, which is typically sRGB.  $\mathbf{M}$  and  $\epsilon_{mn}$  are not disclosed by the manufacturer. However, typically in digital photography, an  $\mathbf{M}$  is applied which yields an sRGB image. We can then replace  $\mathbf{M}\epsilon_{mn}$  by  $\epsilon_{s,mn}$ .

The camera used is sensitive in the wavelength range of visible light  $\Lambda_{visible}$ . Based on our findings of the hardware used, we set  $\Lambda_{visible} = [390 \text{ nm}, 700 \text{ nm}]$ . Other wavelength ranges are expected to be suppressed by an optical filter. Thus, the integration is restricted

to the wavelength interval  $\Lambda_{sensitive} = \Lambda_{visible}$ . Each pixel  $mn$  covers an area  $A_{mn}$  on the sensor chip. Irradiance is assumed to be distributed homogeneously within this small area.

Overall, these considerations yield:

$$S'_{mn} = A_{mn} \Delta t \int_{\Lambda_{visible}} \epsilon_{s,mn}(\lambda) E_{mn,\lambda}(\lambda) d\lambda. \quad (2)$$

Next,  $E_{mn,visible}$ , irradiance in the range of visible wavelengths  $\Lambda_{visible}$ , is estimated based on the three channels of the image which describe the visible spectrum. To this end, first, a gray image is calculated which responds as uniformly as possible to all wavelengths within the visible spectrum.

ASI images are captured using a constant white balance setting. Depending on the color temperature set for white balancing, there is a specific shape of the irradiance spectrum for which pixels respond with identical intensity at each color channel  $c$ . We undo white balancing in order to yield an equal energy image  $S''$ . The equal energy image is yielded weighting each color channel by a factor  $\beta_c$ :

$$S''_{mn,c} = \beta_c S'_{mn,c} \quad (3)$$

The factor  $\beta_c$  indicates the ratio of the response of channel  $c$  when illuminated by a standard daylight spectrum  $E_{\lambda,CT}$  of given color temperature  $CT$  over its response to illumination with white irradiance  $E_{\lambda,white}$ , characterized by a constant spectral irradiance over all  $\lambda$ , using the model from Eq. (2):

$$\beta_c = \frac{\int_{\Lambda_{visible}} \epsilon_{s,mn,c}(\lambda) E_{\lambda,CT}(\lambda) d\lambda}{\int_{\Lambda_{visible}} \epsilon_{s,mn,c}(\lambda) E_{\lambda,white} d\lambda} \quad (4)$$

Only the ratio of the responses of the channels  $c$  is of interest. Accordingly, the constant  $E_{\lambda,white}$  is set to provide  $\sum_c \beta_c = 1$ . In this work  $E_{\lambda,CT}$  is approximated by the spectrum of a blackbody radiator with corresponding (color) temperature. For color temperatures of 5500, 1000 0K,  $\beta$  is determined to [0.3029, 0.3247, 0.3724], [0.3835, 0.3324, 0.2841], respectively.

To measure  $E_{mn,visible}$  exactly from the reading of a pixel  $S'_{mn}$  a large number of color channels  $c$  each with a known and unique spectral sensitivity would be required. Based on the three channels available,  $E_{mn,visible}$  is measured summing the channel intensities  $S'_{mn}$  of the equal energy image and scaling by the calibration factor  $k_{mn}$ :

$$E_{mn,visible} = k_{mn} \beta \cdot S'_{mn}. \quad (5)$$

The pixelwise scaling factor  $k_{mn}$  is typically determined by a radiometric calibration and assumed to be constant for all scenes. In the studied setup  $k_{mn}$  can be determined only based on ASI and pyranometer in an automatic self-calibration by comparing the ASI-derived DHI and the pyranometer's GHI measurement during conditions with zero DNI. This will be explained in more detail later.

A further approximation is required to obtain broadband irradiance. Corresponding with the specification of thermopile pyranometers, broadband irradiance  $E_{mn,bb}$  is defined here as integral of the spectral irradiance  $E_{mn,\lambda}$  over wavelengths  $\Lambda_{bb} = [0.3 \mu\text{m}, 3 \mu\text{m}]$ . Consequently, irradiance received in the visible spectrum  $E_{mn,visible}$ , in which the camera is sensitive, is scaled by a broadband correction  $\beta_{bb}$  to estimate broadband irradiance  $E_{mn,bb}$

$$E_{mn,bb} = \beta_{bb} E_{mn,visible}. \quad (6)$$

Using the SMARTS model (Gueymard, 2005) the spectrum of diffuse irradiance under clear sky conditions  $E_{diffuse,\lambda}$  is calculated and  $\beta_{bb}$  is determined as

$$\beta_{bb} = \frac{\int_{\Lambda_{bb}} E_{diffuse,\lambda} d\lambda}{\int_{\Lambda_{visible}} E_{diffuse,\lambda} d\lambda}. \quad (7)$$

A value of  $\beta_{bb} = 1.56$  is yielded for the calibration conditions used by Wilbert et al. (2016) with an air mass of 1.4 at 500 m over sea level, an aerosol optical depth of 0.1 at a wavelength of 500 nm and precipitable water column of 1.45 cm. The parameter is set constant for all sky conditions. This is a simplification which especially neglects variations in air mass, aerosols and cloud cover. More sophisticated approaches may be tested in the future as discussed below.

Finally, radiance is estimated from the RGB image of the ASI matching each pixel with an area of the sky, which it observes. ASIs are in general geometrically calibrated by an intrinsic and an external calibration. These calibrations allow to map each pixel  $mn$  to a field of view defined by ranges of zenith angle  $\vartheta$  and azimuth angle  $\varphi$  of the sky dome. Radiance  $L$ , integrated over the solid angle  $\Omega_{mn}$  describing the pixel's field of view, constitutes the irradiance received by pixel  $mn$ :

$$E_{mn} = \int_{\Omega_{mn}} L(\vartheta, \varphi) d\Omega \quad (8)$$

Radiance  $L$  is assumed to be constant over the small solid angle  $\Omega_{mn}$  covered by pixel  $mn$ . Thus, a discrete representation of sky radiance  $L_{mn} = E_{mn}/\Omega_{mn}$  is approximated from irradiance  $E_{mn}$  registered by pixel  $mn$ .

### 3.2. Retrieval of diffuse sky irradiance

Diffuse sky irradiance  $D_i(\delta, \phi)$  in a potentially tilted plane is calculated projecting sky radiance into the plane and integrating this projected radiance over the part of the sky dome which is in the plane's field of view  $\Omega_{i,diff}(\delta, \phi)$  (see, e.g. Li and Lam, 2004)

$$D_i = \int_{\Omega_{i,diff}} L \cos \theta_i d\Omega. \quad (9)$$

The evaluated plane is characterized by  $\delta$  and  $\phi$ , which indicate the plane's tilt angle and azimuth angle over north, respectively. The projection is determined by the incidence angle  $\theta_i(\vartheta, \varphi, \delta, \phi)$  between a point in the sky dome  $(\vartheta, \varphi)$  and the plane normal, as defined e.g. by Westbrook (2015).  $\Omega_{i,diff}(\delta, \phi)$  excludes the solid angle of sun disk and circumsolar region. The circumsolar region is defined here as

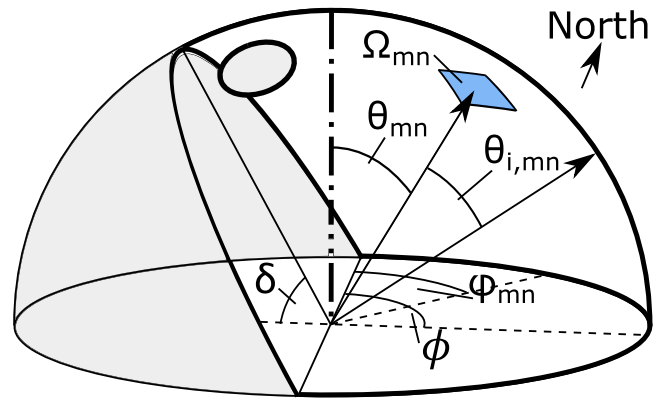


Fig. 2. Solid angle  $\Omega_{mn}$ , zenith angle  $\theta_{mn}$  and azimuth angle  $\varphi_{mn}$  of the sky area registered by pixel  $mn$ . The incidence angle  $\theta_{i,mn}$  of radiance viewed by  $mn$  on a plane with tilt angle  $\delta$  and azimuth angle  $\phi$  is visualized. Solid angles of the sky dome outside the plane's field of view and inside the sun disk which are masked for this plane are shaded exemplarily.

an area of the sky featuring a maximum sun distance angle  $\alpha \leq 2.5^\circ$  which represents the opening angle of common pyrheliometers and the region blocked by a shadow ball over shaded pyranometers.

The incidence angle  $\theta_i$  and  $L$  are approximated as constant over the solid angle  $\Omega_{mn}$  represented by pixel  $mn$ . To simplify the notation,  $MN_i(\delta, \phi) = \{mn | \Omega_{mn} \subset \Omega_{i,diff}(\delta, \phi)\}$  is introduced. In accordance with Li and Lam (2004), the integral from Eq. (9) is written as weighted sum

$$\begin{aligned} D_{i,raw} &= \sum_{mn \in MN_i} \cos \theta_{i,mn} L_{mn} \Omega_{mn} \\ &= \sum_{mn \in MN_i} \cos \theta_{i,mn} E_{mn} \\ &= \beta_{bb} \sum_{mn \in MN_i} \cos \theta_{i,mn} \beta \cdot S'_{mn} k_{mn}. \end{aligned} \quad (10)$$

$E_{mn}$  is calculated by Eq. (6). The subscript *raw* was introduced to distinguish this intermediate measurement from the final measurement which is yielded by corrections introduced in the following section. Relevant geometric relationships are visualized in Fig. 2. The incidence angle  $\theta_{i,mn}$  covered by pixel  $mn$  is known from the intrinsic calibration and external calibration. Diffuse sky irradiance in any arbitrary plane can be measured. Diffuse horizontal irradiance (DHI) is retrieved as  $DHI = D_i(\delta = 0)$ .

Measurement of  $D_{i,raw}$  by Eq. (10) relies on the parameter  $k_{mn}$ . In prior studies,  $k_{mn}$  was determined for each pixel uniquely via a radiometric calibration and assumed to be independent from the observed scene. Accordingly, as a starting point for the more elaborate approaches described next,  $k_{mn}$  is fitted for all pixels uniformly (i.e. dependency on  $mn$  neglected) to minimize the deviation (RMSD) between DHI measured by an ASI ( $DHI_{raw}$ ) and by a shaded reference pyranometer. At PSA, an rRMSD of 20.8%, rBIAS of 6.6% is received for  $DHI_{raw}$ . Fig. 3 evaluates the correlation between reference DHI and  $DHI_{raw}$  by a scatter-density plot. This figure and all other scatter-density plots in this publication evaluate 1 min-average readings. Also, all presented scatter-density plots are also shown in Appendix in a modified version by which the reader can study the models' performances closer. Figs. A.10–A.12 show the relative frequency of the deviation between model and reference over main influences on the models' performance. Fig. 3 shows that the correlation between reference DHI and  $DHI_{raw}$  is not satisfactory, yet. Therefore, further correction terms are introduced as described in the next section.

### 3.3. Correction and calibration of $D_i$ measurements

To improve accuracy over the basic model for  $D_{i,raw}$  from Eq. (10) and to receive one that is more transferable to other times, sites and

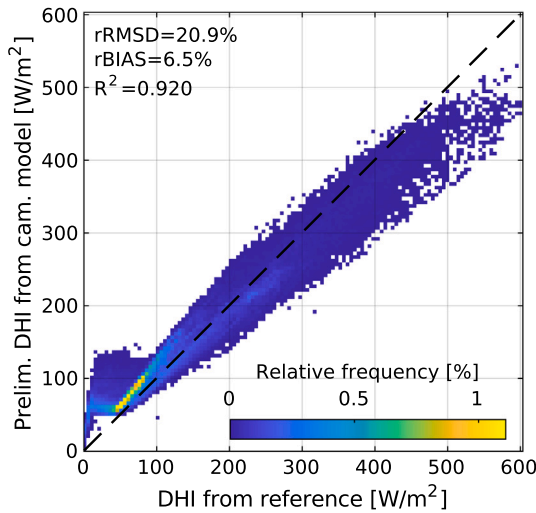


Fig. 3. Intermediate result,  $DHI_{raw}$ , from ASI image over reference DHI (1 min-averages) in the development period at CIEMAT'S PSA (2019-07-01 through 2019-12-31). As starting point for more elaborate approaches, a constant  $k_{mn}$  was fit based on this dataset.

instruments, the model equation and  $k_{mn}$  are adapted. In Fig. 3, we see a relatively broad scatter, especially for low DHI, and a nonlinearity. To solve this,  $k_{mn}$  is modeled by two multiplicative parameters:

$$k_{mn} = k_{exp} * k_{sens}. \tag{11}$$

where  $k_{exp}$  depends on the exposure and describes the variable effect of the camera firmware's internal exposure control on the camera's sensitivity.  $k_{sens}$  indicates a static sensitivity of an individual camera. Both factors are scalars applied uniformly for all pixels  $mn$ . The determination of  $k_{exp}$  and  $k_{sens}$  is described in Sections 3.3.1 and 3.3.2, respectively. This simplification neglects vignetting — the possibly reduced sensitivity of the camera near the boundary of its field of view. Prior works, which aimed to measure sky radiance by ASIs, usually applied a radiometric calibration which also compensated vignetting. However, following the reasoning of Chauvin et al. (2015), we expect that vignetting is explained majorly by differences in the solid angles viewed by pixels for a fish eye lens. As this influence is covered by geometric calibrations in the present study, a possibly remaining vignetting effect is neglected.

Further, Eq. (10) is extended by an additive correction factor  $k_{add}$ , which yields the final measurement:

$$D_i = \underbrace{\beta_{bb} k_{mn} \sum_{mn \in MN_i | \alpha(m,n) \geq 25^\circ} \cos \theta_{i,mn} \sum_c \beta_c S'_{mn,c}}_I + \underbrace{\max(0, \beta_{bb} k_{mn} \sum_{mn \in MN_i | \alpha(m,n) < 25^\circ} \cos \theta_{i,mn} \sum_c \beta_c S'_{mn,c} + k_{add})}_{II}. \tag{12}$$

To account for two superimposed mechanisms, which are expected to influence the image acquisition near the sun, the additive correction is designed as:

$$k_{add} = k_{sat} n_{sat} - k_{glare} DNI. \tag{13}$$

DNI required in Eq. (13) is calculated based on GHI from the pyranometer and DHI from the camera image by the fundamental relationship

$$DNI = (GHI - DHI) * \cos^{-1} \theta_{i,b} (\delta = 0). \tag{14}$$

where  $\theta_{i,b}(\delta, \phi)$  is the incidence angle of DNI for the evaluated plane, in this case for the horizontal plane ( $\delta = 0$ ). For the correction, DNI is

calculated substituting DHI with  $DHI_{raw}$  in the above equation. Where  $DHI_{raw}$  is only corrected with  $k_{mn} = k_{exp} * k_{sens}$ .

The camera's limited dynamic range causes saturation for a number of pixels  $n_{sat}$  in the proximity of the sun, even outside the circumsolar region defined for the evaluation. Especially during cloud enhancement events, diffuse irradiance is then underestimated.  $k_{sat}$  accounts for this effect. On the other hand, lens glare causes a part of DNI to be spread over wider areas of the ASI image, which appear bright and may feature characteristic rays. Consequently, diffuse irradiance is overestimated by a fraction  $k_{glare}$  of DNI.

In Eq. (12), the sum over all pixels in a plane's field of view  $MN_i$  was split into one sum for pixels viewing the sky at sun distance angles  $\alpha$  smaller than  $25^\circ$  and one sum over the remaining pixels. The sum was separated as it is expected that image saturation and lens glare mostly affect the measurement up to this sun distance angle, while we do not know where exactly inside this solid angle radiance is estimated incorrectly. The second summand in Eq. (12) corresponds to irradiance received from the solid angle with  $\alpha < 25^\circ$ . By the *max*-function, we assure that this fraction of irradiance is at least zero in any situation and for any evaluated plane. Before applying *max*, a large value of the glare correction could let this irradiance component become negative. To be most accurate,  $n_{sat}$  should be calculated only from saturated pixels inside a plane's field of view. However, in this study,  $n_{sat}$  is calculated from the ASI's entire field of view. Meteorological data used in this study are processed at a temporal resolution of 1 min (averages representing e.g. 14:01:01 through 14:02:00). The ASI provides two instantaneous readings per minute (e.g. 14:01:30 and 14:02:00). For every raw parameter received from the ASI, these two samples are averaged to represent a 1 min-average reading. These two samples may not be completely representative of the 1- min reporting interval. Averaging is applied before any corrections are computed. E.g.  $n_{sat}$  and the terms  $I, II$  in Eq. (12) are averaged before further processing.

### 3.3.1. On-the-fly adaption of the camera sensitivity parameter $k_{exp}$

To determine  $k_{exp}$  we use illuminance data. The fisheye camera used, just as many other commercial cameras which may qualify as all-sky imager, provides a measurement of illuminance. Simultaneously illuminance can be estimated from the ASI image. The comparison of both readings allows to understand the effect of the camera's exposure control on image intensity. Moreover, the comparison of both readings allows to determine  $k_{exp}$  dynamically and on-the-fly.

First, illuminance is calculated from the ASI image. In analogy to the measurement of irradiance (Eq. (12)), illuminance received by a pixel reads

$$I_{mn} = 683 \text{ lux}/(\text{W}/\text{m}^2) k_{exp} \sum_{c \in \{R,G,B\}} v_c \beta_c S_{mn,c}. \tag{15}$$

However, from the correction terms  $k_{exp}, k_{sens}, k_{sat}, k_{glare}$ , only  $k_{exp}$  is applied in this step. The ASI-firmware is expected to calculate illuminance correcting for influences induced by its internal exposure control and digital image processing. These corrections are represented by  $k_{exp}$ . In contrast, the remaining correction parameters are related to the camera's optical and electronic hardware and cannot be expected to be known to the ASI-firmware.  $v_c$  indicates the mean luminous efficiency of channel  $c$ . Assuming an sRGB image and based on the definition of sRGB (International Electrotechnical Commission, 1999),  $v_c = [0.2126, 0.7152, 0.0722]$  is used, while this definition supposes a white point of 6500 K. As before for irradiance, illuminance received by a pixel can be written as

$$I_{mn} = \int_{\Omega_{mn}} L_v(\theta, \varphi) d\Omega \tag{16}$$

Illuminance registered by the camera is derived as the integral over the camera's field of view  $\Omega_{cam}$ :

$$I_{img} = \int_{\Omega_{cam}} L_v d\Omega = \sum_{mn} I_{mn}. \tag{17}$$

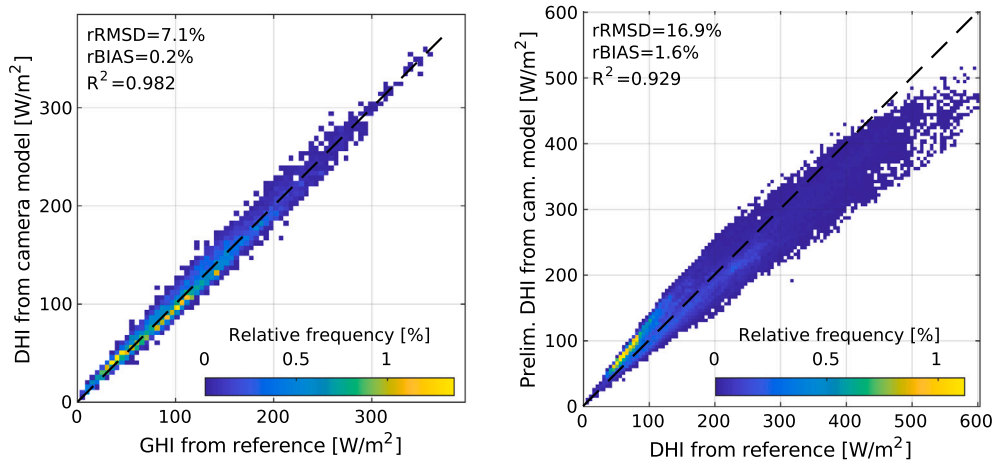


Fig. 4. Intermediate results for DHI from ASI images (1 min-averages) in the dataset retrieved at CIEMAT’s PSA, corrected with illuminance on the fly. Left: Comparison of ASI-based DHI to GHI from unshaded pyranometer restricted to situations with less than 100 saturated pixels in the ASI image. These situations are used to calibrate  $k_{sens}$ .  $k_{add}$  is set to zero which is adequate for these conditions. Right: Comparison of ASI-based and reference DHI for all data points in the development period.  $k_{add}$  is set to zero in this step, but is applied for the final DHI from the ASI.

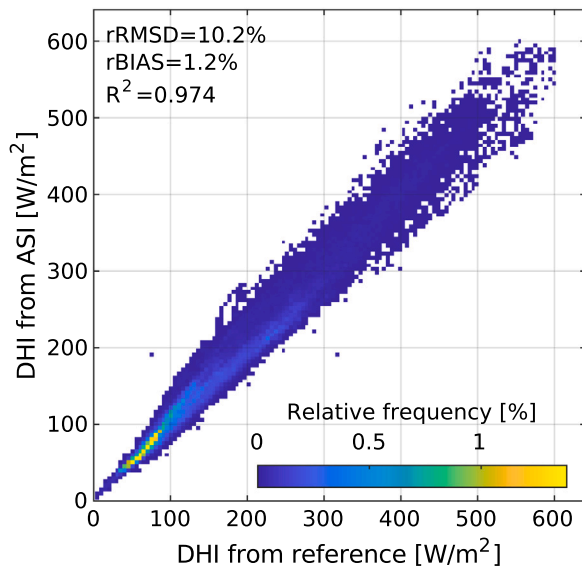


Fig. 5. Final DHI from ASI image in the dataset retrieved from CIEMAT’s PSA (1 min-averages), including glare correction and correction for image saturation over reference DHI, restricted to time stamps from the development period (2019-07-01 through 2019-12-31).

Projection into the sensor plane, i.e. multiplication of  $L_v$  with  $\cos \theta_i$ , is necessary to receive actual illuminance for the plane the camera is mounted in (see, e.g. Inanici, 2010). However, this multiplication is not considered by the camera firmware, as tests showed, and therefore needs to be neglected also in our calculation.

Illuminance computed from the image  $I_{img}$  and provided by the camera firmware  $I_{ref}$  were compared for the dataset from PSA, restricted dates in 2019-07-01 to 2019-12-31. In the following, this period serves as *development period*. For  $I_{ref} > 12000$  lux except for a constant scaling factor, both measurements coincide very well. This very strong correlation indicates small interference of the camera control in the image acquisition in these cases. On the contrary, for  $I_{ref} \in [1600, 12000]$  lux,  $I_{img}$  remains nearly constant at around 12000 lux. This is caused by a camera control strategy that keeps the brightness of images from dark scenes at a constant minimum level by applying an analogue gain of increased magnitude before digitalization. This control strategy keeps the signal-to-noise ratio in low light situations

high. For very dark scenes ( $I_{ref} < 1600$  lux),  $I_{img}$  decreases linearly and coincides with  $I_{ref}$  in the origin for complete darkness. In these situations the applied analogue gain is apparently already at its maximum. A further decrease of illuminance can therefore not be compensated and image brightness reduces.

We use  $I_{ref}$  to correct the irradiance measurement on the fly. For each time stamp, we automatically set the correction factor to

$$k_{exp} = I_{ref} / I_{img}. \quad (18)$$

For this correction it is not of foremost importance how accurately  $I_{ref}$  represents the actual illuminance of the scene. More importantly,  $k_{exp}$  serves as indicator of camera-internal gains which are increased during dark conditions. The correction is expected to be most relevant in overcast and twilight situations. For the development period, the correction reduces relative standard deviation of the measurement by more than 3% and improves the correlation with the reference measurement.

### 3.3.2. Online determination of camera sensitivity by a coupled pyranometer

The combined setup of ASI and pyranometer allows to continuously calibrate the sensitivity of the ASI: In diffuse conditions ( $DNI = 0$   $W/m^2$ ), GHI should equal DHI. A diffuse situation is identified from the ASI image if the number of saturated pixels is smaller than 100 (i.e. 0.0023% of all pixels). In the development at PSA, this threshold was found to filter out situations with  $DNI > 0$   $W/m^2$  reliably. After a sufficient number of scenes with zero DNI has been observed,  $k_{sens}$  is selected which minimizes the RMSD between GHI and DHI for this filtered dataset. For these diffuse situations, additive corrections  $k_{add}$  in Eq. (12) are very close to zero: By our definition  $n_{sat}$  is very small; simultaneously DNI is low, which avoids glare effects. Consequently,  $k_{add} = 0$   $W/m^2$  is set as an approximation during this calibration.

For PSA  $k_{sens} = 0.408$  is obtained. DHI from ASI after correction by illuminance and self-calibration is compared to GHI for such diffuse situations in Fig. 4 left. Both measures agree well under these conditions, while at a temporal resolution of 1 min still some scattering is observed, yielding an rRMSD of 7.1%. Fig. 4 right visualizes the coincidence of the reference  $DHI_{Ref}$  and the ASI-based  $DHI_{ASI}$  after applying  $k_{exp} * k_{sens}$  for the complete development period.  $DHI_{ASI}$  correlates much better with the reference than  $DHI_{raw}$ . From the comparison of Figs. 3 and 4, the dynamic correction by  $k_{exp}$  removes a strong positive bias, which is seen prior to the correction if  $DHI_{ref} < 50$   $W/m^2$ . As diffuse situations are found automatically by this method without any further information,  $k_{sens}$  can by this method be determined for any other ASI and at an unknown site.

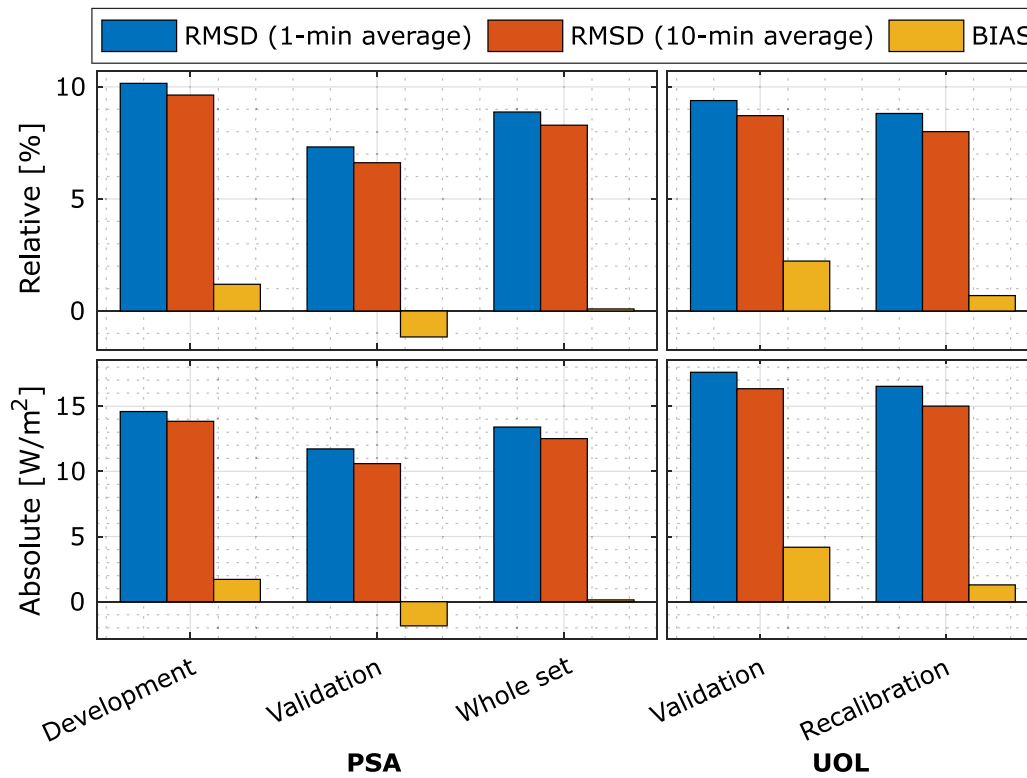


Fig. 6. Absolute and relative deviation metrics of DHI measured by the ASI-based method validated with DHI from a shaded thermopile pyranometer at CIEMAT’s PSA (left) and UOL (right). At PSA, deviation metrics are distinguished between datasets and at UOL between separate sets of model parameters determined by self-calibration and a recalibration using reference measurements, respectively.

### 3.3.3. Image saturation

A shortcoming of the commercial fisheye surveillance cameras used as ASIs lies in these cameras’ limited dynamic range. Therefore, images frequently feature saturation in the circumsolar area. Large turbidity and optically very thin clouds increase scattering of beam irradiance which leads to the impression of a large sun disk in the image. Furthermore, clouds reflect solar irradiance during enhancement events. These clouds may also appear saturated in the ASI image.

In parts of the sky dome, which correspond to such saturated pixels, radiance is underestimated. Consequently, in situations with image saturation,  $D_i$  is also underestimated. In this study, the effect was analyzed by the relative frequency at which pairs of deviation  $DHI_{ASI} - DHI_{Ref}$  and a specific number of saturated pixels  $n_{sat}$  were observed. This examination suggested an additive error that scales linearly with the number of saturated pixels  $n_{sat}$ . As this coarsely meets the expected effect of image saturation, the term  $k_{sat} * n_{sat}$  was included in Eq. (13). The parameter  $k_{sat}$  is estimated by multivariate regression, which is performed jointly for the parameters  $k_{sat}$  and  $k_{glare}$ . RMSD between ASI-based final DHI and reference DHI was used as loss to be minimized. Based on the PSA dataset used for development,  $k_{sat} = 4.6 * 10^{-4} W/m^2/pixel$  is determined. The correction factor is held constant between sites and despite the differences in camera hardware and settings at PSA und UOL. Our tests showed that  $k_{sat}$  is reproduced qualitatively at both sites and for both instruments. Based on this, we expect that  $k_{sat}$  can also be transferred to other sites. Additionally,  $k_{sat}$  has a comparably small influence on measurement accuracy. Hence, we expect that it is sufficient to specify its value approximately.

### 3.3.4. Lens glare

Common ASIs capture the entire sky dome without any shading device. This setup is prone to glare effects in the presence of direct irradiance. These effects can introduce a positive bias of measured radiance near the sun as shown in Meija et al. (2016). Glare from a pointwise light source is expected to disperse radiance from this point

over a wider image area. It is conclusive that scattered beam irradiance scales linearly with beam irradiance and that it superimposes the actual sky radiance which is of interest. This motivates the used additive glare correction in Eq. (13). Fig. 4 (right) exhibits two separate clusters. One rather dense cluster is seen above the main diagonal. The second cluster is more disperse but centered on the main diagonal. For each cluster, a correlation of DHI from reference and camera is seen, but with a slightly different slope. The separation is traced back to the influence of direct irradiation and supports the correction used. This was also observed by Kurtz and Kleissl (2017) for measurement of DHI based on an ASI image.

The magnitude of lens glare is likely to depend on the optical properties of the camera lens. Therefore, we aim to determine  $k_{glare}$  for each individual camera model and each individual camera based on clear-sky periods using only the combination of ASI and pyranometer. GHI timeseries are screened for potentially clear periods. In the second step, ASI images of these periods are inspected and only periods with very low cloud coverage are retained. These steps are carried out manually but may easily be automated by cloud segmentation techniques which are able to detect such clear skies reliably (e.g. Fabel et al., 2021).

For the remaining clear sky periods GHI, DNI and from these also DHI are modeled by the Ineichen clear sky irradiance model (Ineichen and Perez, 2002), which only relies on Linke turbidity, the present solar geometry and the location’s altitude. For each clear sky period a numerical solver is applied to find a pair of Linke turbidity and  $k_{glare}$  which minimizes the sum of the MADs of measured versus modeled GHI, DNI and DHI, respectively. MAD is assumed to respond less strongly to outliers. This is considered to be advantageous when few timestamps featuring clear-sky are available for this calibration. As start value in the minimization, a Linke turbidity of 2 and  $k_{glare} = 0.030$  are applied. As described in Section 3.3.3, the start value of  $k_{glare}$  is derived by multivariate regression of  $k_{glare}$  and  $k_{sat}$  based on DNI and DHI from a solar tracker setup. Lastly, the median of the  $k_{glare}$  values determined over all clear sky periods is accepted as final estimation of  $k_{glare}$ . On the

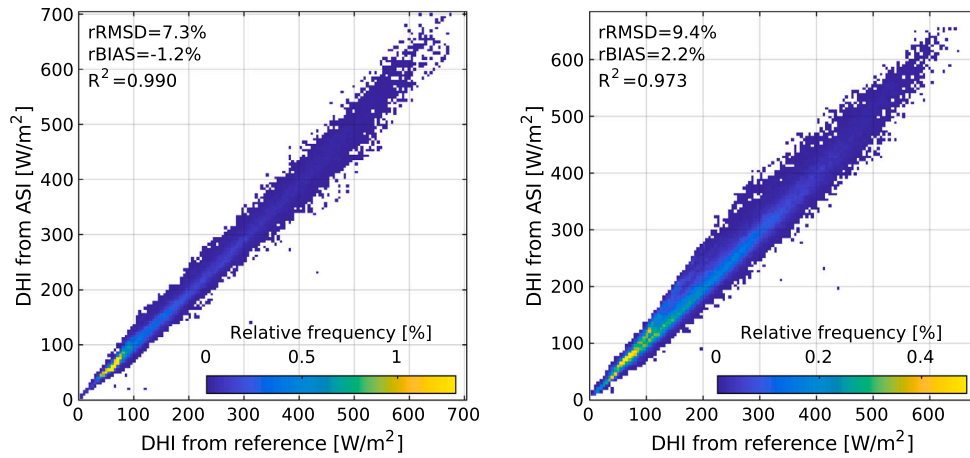


Fig. 7. Relative frequency of observed pairs of DHI measured by the ASI-based method and by the shaded reference pyranometer (1 min-averages) at CIEMAT's PSA (validation period, left) and UOL (right).

basis of clear sky periods from 46 days distributed over the development period,  $k_{glare} = 0.028$  is determined and used in the following.

In the development and in the validation presented later, DNI used as input for glare correction is computed by Eq. (14), using the preliminary DHI, which was not yet corrected for glare. For the subsequent estimation of final DHI,  $D_t$  and GTI the calculation of DNI is repeated with the corrected DHI.

The final coincidence of DHI measured by ASI and reference is presented in Fig. 5. The graph shows that both additive corrections together significantly improve measurement accuracy. The correction for image saturation compensates a negative bias and increased scattering found for large values of reference DHI ( $DHI_{ref} \in [300, 600]$  W/m<sup>2</sup>). As expected, glare correction unites the separate clusters found for the measurement of DHI without additive corrections. The self-calibration of lens glare presented here can be applied regularly or online without additional hardware. This way, the method can compensate for differences between individual ASI lenses and also for aging of the ASI lens coating.

### 3.4. Global horizontal, global tilted and beam irradiance

A thermopile pyranometer placed in a horizontal plane delivers global horizontal irradiance (GHI) at comparably high accuracy. Direct normal irradiance (DNI) is computed from the pyranometer's GHI and ASI-derived DHI using Eq. (14).

To obtain GTI ( $\delta, \phi$ ), DNI is projected into the evaluated plane. Consecutively, this component together with diffuse sky irradiance  $D_t$  and ground reflected irradiance  $D_g$  in the evaluated plane constitute GTI:

$$GTI = DNI * \cos \theta_{i,b} + D_t + D_g. \quad (19)$$

Assuming isotropy of reflected irradiance,  $D_g$  is computed simply from GHI and ground albedo  $\rho$  (see, e.g. Demain et al., 2013; Yang, 2016):

$$D_g = \frac{1 - \cos(\delta)}{2} * \rho * GHI. \quad (20)$$

The method presented here can analogously include GTI from a tilted pyranometer instead of GHI. Note that, especially for retrieval of DNI, the sun position is required to be within the pyranometer plane's field of view  $\Omega_{t,diff}$ .

## 4. Validation

The method to measure DHI and GTI based on a combined setup of pyranometer and ASI (in the following referred to as ASI-based method) was developed based on the months July to December 2019

(development period) in Section 3. In the following, the method is first tested by applying it to the consecutive six months (validation period) and in the next step by applying it to site UOL. Thereafter, GTI measured by the ASI-based method is benchmarked over state-of-the-art approaches at both sites and for the respective periods. At PSA, the initial calibration is kept also for the validation period. At UOL, the self-calibrations relying only on ASI and pyranometer are applied to the measurement, based on the very clear and diffuse periods contained in the dataset. If the procedure is applied in the field, the self-calibrations may be updated continuously every night or applied retrospectively, as in the present case. In any case the calibration parameters should be determined over a sufficiently long period which includes multiple very clear periods as well as diffuse periods. To account for a possible wear-off and aging of the camera optics and sensors, we suggest to revise and update the self-calibration annually.

We define absolute and relative deviation metrics between test measurement  $y_{Meas}$  and reference  $y_{Ref}$  according to

$$RMSD = \sqrt{\frac{1}{N} \sum_{i=1}^N (y_{Meas,i} - y_{Ref,i})^2},$$

$$BIAS = \frac{1}{N} \sum_{i=1}^N (y_{Meas,i} - y_{Ref,i}),$$

$$\overline{y_{Ref}} = \frac{1}{N} \sum_{i=1}^N y_{Ref,i},$$

$$rRMSD = RMSD / \overline{y_{Ref}} \times 100\%,$$

$$rBIAS = BIAS / \overline{y_{Ref}} \times 100\%.$$

Time stamps for which any of the data sources does not provide valid readings are excluded from the validation. The largest part of time stamps sorted out go back to reduced data quality of reference data. Both products DHI and GTI are examined by these deviation metrics and by scatter-density plots that visualize the coincidence of reference and model under different sky conditions. Additionally, Appendix shows these scatter-density plots in a modified version which evaluates the deviation between modeled DHI or GTI and reference DHI or GTI over reference DHI or GTI.

### 4.1. Diffuse horizontal irradiance

DHI measured by the ASI-based approach is validated against DHI measured by a thermopile pyranometer shaded by a tracked shadow ball. The deviation metrics for the measurements at UOL and at PSA are presented in Fig. 6, using the original resolution of 1 min as well as a 10 min sliding average. For the latter site, metrics in Fig. 6

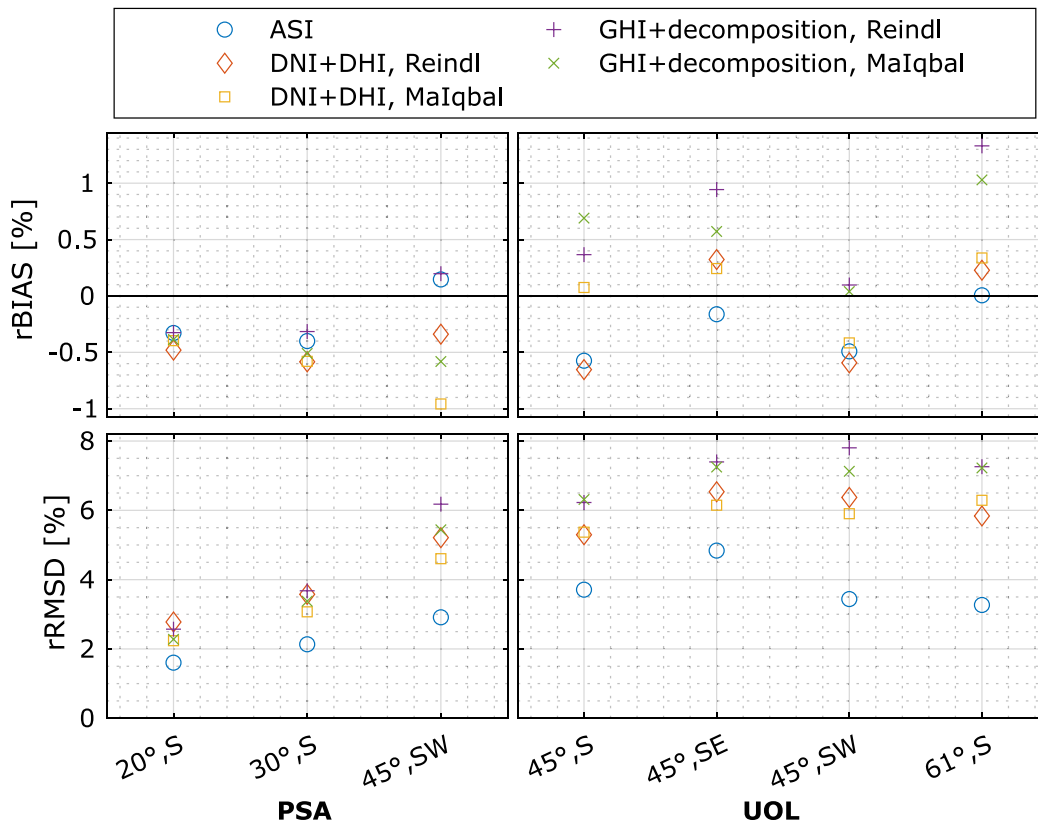


Fig. 8. Deviation metrics (rBIAS top, rRMSD bottom) received for GTI (10 min average) in specified planes, left CIEMAT's PSA, right UOL.

are distinguished between *development* and *validation* period and the combination of both periods (*whole set*), respectively. Measurements at UOL, described here and in Section 4.2, are performed by applying the self-calibrations described in Section 3.3 (Fig. 6, *UOL validation*). Only for  $k_{sat}$  no self-calibration procedure is available, which is why the value found at PSA is retained. Further, Fig. 6 *UOL recalibration* evaluates deviation metrics for the UOL dataset, while recalibrating the model parameters via reference data instead of the self-calibration.

At PSA, RMSD is actually smaller for the half year of validation compared to the half year of development. This may indicate that meteorological conditions in the half year of validation are more favorable for the method. The model parameters were only determined to minimize RMSD during the development phase. However, interestingly, BIAS is almost zero if both periods, development and validation, are combined (whole set in Fig. 6).

A recalibration based on the validation period at PSA yields very similar calibration parameters. This indicates good transferability to other periods. rRMSD at the validation site UOL is in the range found for PSA. rBIAS and the metrics in absolute values, RMSD, BIAS, are both moderately larger at site UOL. Based on this, the method can be transferred reasonably well to another site and type of ASI. The comparison further shows that rBIAS changes between sites and also between the periods evaluated at PSA. Based on this, variations in the atmospheric conditions may cause a moderate systematic deviation. The analysis of RMSD is also performed for 10 min-resolution. Small reductions of rRMSD between 0.5% and 0.8% are found. The larger RMSD at 1 min-resolution can be related to the ASIs' large sampling interval of 30 s. These two samples may not represent the 1-min reporting interval sufficiently. In particular, the use of two samples per minute (half and full minute) is expected to cause a mismatch between the time intervals represented by ASI-based and radiometer-based data. In a future application, the ASIs should be operated at an increased sampling rate or alternatively three samples should be averaged weighting the reading from the previous full minute (e.g. 14:01:00) by 0.25,

Table 2

Mean values of reference DHI at the sites PSA and UOL for the respective datasets.	
Site, dataset	Mean irradiance [W/m <sup>2</sup> ]
PSA, calibration period	144
PSA, validation period	160
PSA, whole set	151
UOL	187

the reading from the present half minute (e.g. 14:01:30) by 0.5 and the present full minute (e.g. 14:02:00) by 0.25.

Scatter-density plots of ASI-based versus reference DHI are shown in Fig. 7 for the validation periods at PSA (left) and at UOL (right). For both sites very few readings deviate strongly from the reference. The comparison in Fig. 7 is obviously influenced by differences in the local meteorological conditions. Reference DHI at UOL is distributed over a wider range of values compared to PSA. Additionally from our experience, at PSA, large readings of reference DHI often occur in turbid situations or in the presence of optically thin high layer clouds. For UOL, these high values are more often connected to enhancement events in the presence of optically thick clouds. The mean values of DHI (see Table 2) are similar between the datasets. The variation of the mean value of DHI qualitatively reflects the variation of RMSD between datasets.

The model parameters  $k_{sens}$  and  $k_{glare}$  were self-calibrated at site UOL, which yielded 0.373 and 0.052, respectively. However, if we calibrate based on reference DNI from the pyrhelimeter and reference DHI from the shaded pyranometer instead,  $k_{glare} = 0.06$  and  $k_{sat} = 4.3 \cdot 10^{-4} \text{ W/m}^2/\text{pixel}$  are obtained. The inaccurate estimation of  $k_{glare}$  would mostly explain the weaker performance of the DHI measurement at site UOL in terms of BIAS and RMSD. On the other hand,  $k_{sat}$  approximately matches the value  $k_{sat} = 4.6 \cdot 10^{-4} \text{ W/m}^2/\text{pixel}$  found at PSA. These parameters reflect that the procedure to estimate the glare correction on-site should be improved to further increase the

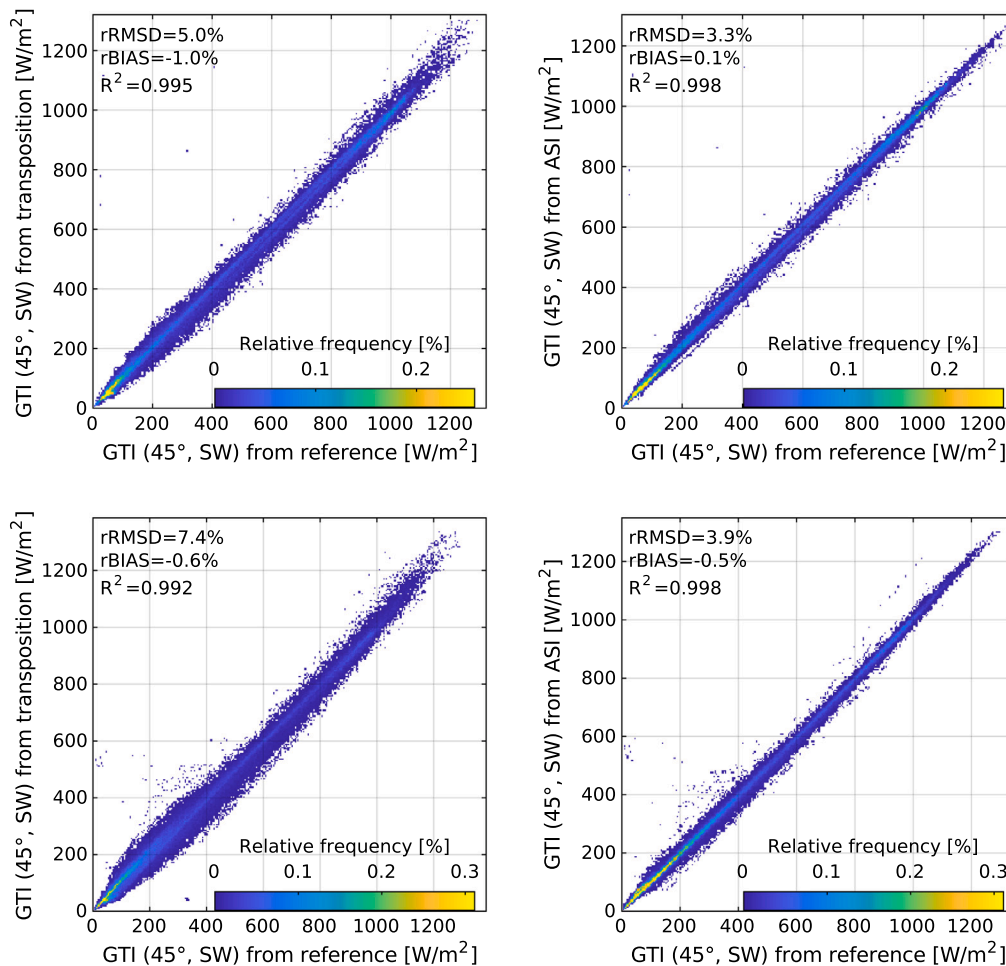


Fig. 9. Relative frequency of observed pairs of GTI from model and reference in a plane with tilt 45°, orientation southwest, temporal resolution of 1 min-average: top left transposition model Ma-Iqbal (Demain et al., 2013) based on DNI, DHI from solar tracker at CIEMAT's PSA, top right ASI + pyranometer at CIEMAT's PSA, bottom left transposition model Reindl (Yang, 2016) based on DNI, DHI from solar tracker at UOL, bottom right ASI + pyranometer at UOL.

transferability of the proposed method. If the parameters are recalibrated based on DNI from the pyrheliometer, i.e. setting  $k_{glare} = 0.06$  and  $k_{sat} = 4.3 \cdot 10^{-4} \text{ W/m}^2/\text{pixel}$ , the ASI-based measurement and reference measurement of DHI correlate very similar as found for PSA (see rightmost bar-plots in Fig. 6).

Meteorological conditions influence the measurement also through the spectral composition of diffuse irradiance, i.e. through  $\beta_{bb}$  defined by Eq. (7).  $\beta_{bb}$  is expected to vary significantly, within 1.43 ... 1.95, as aerosol optical depth (0.01 ... 0.5), precipitable water column (0.11 cm ... 3.5 cm) and air mass (1 ... 4) may range within the intervals in brackets.

Additionally, clouds filter spectral irradiance more effectively at higher wavelengths according to Nann and Riordan (1991). These effects cause a varying sensitivity of the measurement depending on sky conditions and occur in a similar way for Rotating Shadowband Irradiometers (RSI). As described by Wilbert et al. (2016), such spectral deviations seen for RSI can in part be corrected, yielding significant improvements in accuracy. Based on that, the simplified broadband correction is expected to explain a significant share of the deviations found for the present method, including a part of the deviations related to the presence of beam irradiance. A more elaborate correction may reduce these deviations in the future, especially if parameterized by the ratio of the RGB-intensities in the ASI-image.

The test sites of this study feature very different climates as discussed in Section 2. At least for Europe, PSA and UOL represent extreme cases in particular regarding cloud-coverage. Consequently, we expect that the method presented here also works at sites with a climate

between these extremes. However, not all environmental conditions can be tested at the sites. Conditions with snow and frost are not represented notably in any of the datasets. Periods with increased aerosol load related to Sahara dust occur sporadically at PSA. Still, at desert sites such as Dubai or in metropolises like Mumbai, very turbid conditions are expected to be frequent. We expect that the method will also be valid for strongly different climates because of the physical approach. However, the accuracy might be slightly reduced in particular due to the still simplistic use of the three color channels of the camera.

#### 4.2. Global tilted irradiance

Global tilted irradiance (GTI) measured by the ASI-based method is validated using thermopile pyranometers in distinct planes. Additionally, the method is benchmarked over four state-of-the-art approaches to estimate GTI with transposition models based on DNI and DHI or based on decomposition and transposition models using GHI alone. DNI and DHI measured by pyrheliometer and shaded pyranometer of the tracker setup are transformed into GTI using the Ma-Iqbal and Reindl transposition models (Demain et al., 2013; Yang, 2016). Additionally, GTI is computed with these models while relying on DNI and DHI received from decomposition of GHI. The decomposition is performed by the DIRINT-model with time-series improvement and including measured air temperature and relative humidity as implemented in pvlib. The selected transposition models Reindl and Ma-Iqbal were previously found to be among the most accurate ones for site UOL based

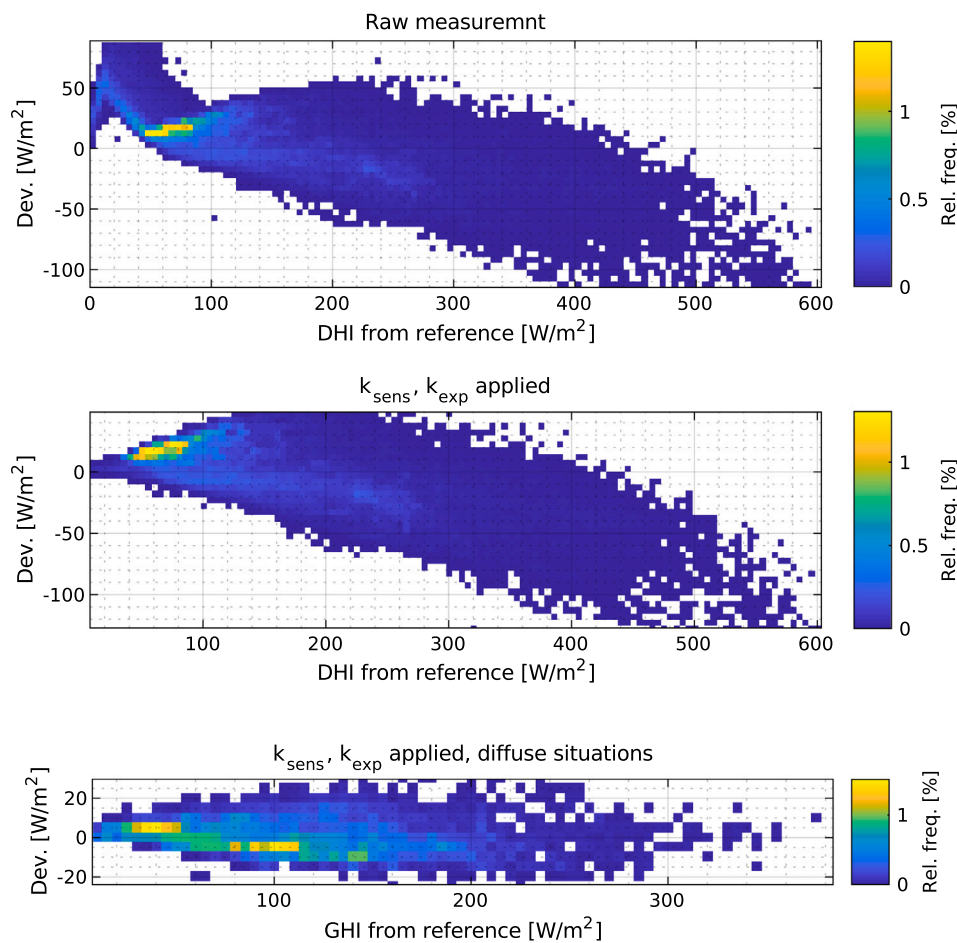


**Fig. A.10.** Relative frequency of the observed deviation (Dev.) between preliminary ASI-based DHI and reference DHI over reference DHI or GHI, temporal resolution of 1 min-average, at CIEMAT’s PSA for the calibration dataset: raw ASI-based measurement applying only a static calibration factor (top), applying  $k_{sens}$  and  $k_{exp}$  (center row), applying  $k_{sens}$  and  $k_{exp}$  restricted to diffuse situations with  $DNI \approx 0$  (bottom).

**Table 3**

Mean global tilted irradiance (GTI) in the planes used in the validation specified by site, tilt and orientation. For site PSA, this validation only includes the validation dataset.

Site, tilt, Orientation	GTI [W/m <sup>2</sup> ]
PSA 30°, S	525
PSA 20°, S	518
PSA 45°, SW	475
UOL 45°, S	396
UOL 45°, SE	383
UOL 45°, SW	371
UOL 61°, S	364

on Yang (2016) and based on a previous unpublished benchmark at PSA, respectively.

Fig. 8 shows deviation metrics received for each of these methods evaluating the validation dataset of PSA (left column) and the dataset of UOL (right column), respectively. Mean irradiances in the planes are listed in Table 3. At both sites, rBIAS (Fig. 8, top row) is moderate for all used models and planes. Only the use of decomposition and consecutive transposition delivers a significant rBIAS  $\approx 1.3\%$  for the plane with a tilt of 61° at UOL. Uncertainties in the calibration of the included radiometers are expected to contribute a considerable share of rBIAS as these bias errors are mostly below the calibration uncertainty of pyranometers (Vuilleumier et al., 2014). Likewise, unknown albedo of the near field can induce a part of the rBIAS at both sites. At PSA,

an albedo measurement is currently being set up directly next to the ASI. This will allow us to validate the albedo.

Another influence may be an inaccurate alignment of the radiometers. The azimuth angles of pyranometers installed in south-facing planes were examined based on single clear sky days. For these days, the GTI timeseries were expected to be symmetric around solar noon, given that both timeseries of DNI and GHI were symmetric also. In a first order approximation, a small deviation in a plane’s azimuth angle was translated into a temporal shift of the GTI timeseries before and after noon. For the planes at PSA and the plane 61°, S at UOL, this test indicated a deviation of 0.5...1°. A larger deviation of  $-2^\circ$  was suggested for the plane 45°, S at UOL. To test the influence of this apparent deviation, the estimated azimuth angle of the plane was modified accordingly. The performance of the models did not change significantly in comparison to one another, in the test. Meanwhile, the metrics of all used models consistently indicated a significant gain in accuracy. For the ASI-based model, GTI in the plane UOL-45°, S is then predicted with an rRMSD of 2.9% and an rBIAS of  $-0.5\%$ . All planes at UOL, which are tilted by 45°, are mounted on the same structure. Simultaneously, these planes exhibit among the largest deviations for the tested models. Therefore, it is likely, that an inaccurate alignment affects the performance of all approaches for these planes. As only south-facing planes could be checked in this way and as the test may only estimate misalignments roughly, we waived this correction in the validation.

While discussed influences are likely as most models exhibit a similar variation of rBIAS with the orientation of the planes, the magnitude

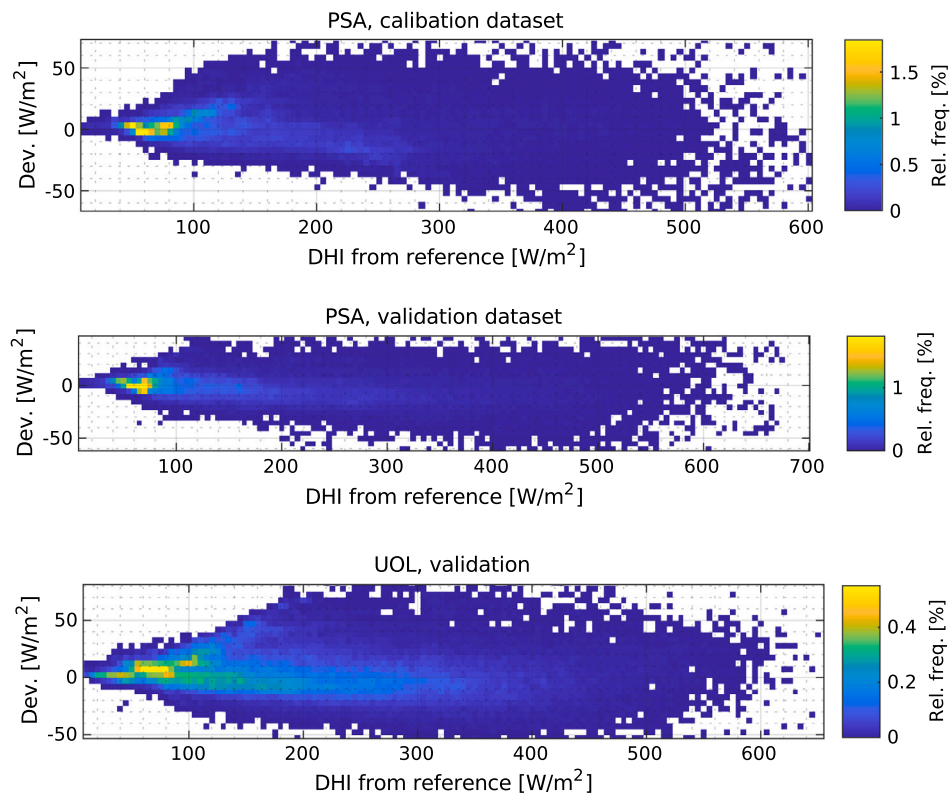


Fig. A.11. Relative frequency of the observed deviation (Dev.) between the final ASI-based DHI and reference DHI over reference DHI, temporal resolution of 1 min-average: At CIEMAT's PSA for the calibration dataset (top), at PSA for the validation dataset (center row), in the validation at UOL (bottom).

of rBIAS complies well with the literature for studied transposition models relying on measured DNI and DHI (e.g. Yang, 2016).

The rRMSD of GTI is shown in Fig. 8 (bottom row). At both sites, rRMSD of GTI predicted by transposition models increases with the tilt of an evaluated plane. This increase is more pronounced if decomposition provides DNI and DHI for the transposition. The ASI-based prediction of GTI is more accurate in terms of rRMSD for all studied planes at both sites compared to the transposition models relying on DNI and DHI from either the tracker setup or from decomposition. The advantage of the ASI-based prediction increases with the tilt angle. Our results may further indicate that deviations of the ASI-based method only increase slightly with the tilt of the evaluated plane. However, the reference measurements are not sufficiently accurate to study this indication in more detail.

Coincidence of predicted and reference GTI for the plane with 45° tilt and orientation southwest is visualized by scatter-density plots in Fig. 9. The left column compares transposition models to the reference: The best model for each of the two sites is shown, Ma-Iqbal for PSA top left and Reindl for UOL bottom left. The right column compares ASI-based measurement to reference. The top row evaluates PSA, the bottom row UOL. At PSA, the reference GTI is distributed rather homogeneously over the range of values to be expected. At UOL, low-GTI situations are dominant. The rather moderate deviations found before for all of the tested models are reflected by the scatter-density plots. Grid cells with any and especially with large relative frequencies are well aligned with the main diagonal. Measurements from the ASI-based method exhibit lower scattering over the respective transposition models. This reduction is clearest at this high temporal resolution of 1 min. Fig. A.12 allows to study the deviations of the ASI-based method and the transposition models in more detail.

In this evaluation, ASI-based measurement of GTI was tested against transposition based on DNI and DHI from a tracker setup equipped with thermal pyrheliometer and shaded pyranometer. This very accurate

measurement of DNI and DHI is expected to constitute the most challenging opponent to benchmark against. We expect that more practical and economical but less accurate measurement setups, especially based on RSI or SPN1, will be outperformed even more clearly. Additionally, the proposed method to measure GTI is benchmarked over transposition models which were found most suited for the studied sites in prior tests. In the field, the advantage of the ASI-based method may be even more pronounced, as the transposition model, which is most suited to a site, is not known in advance.

## 5. Conclusion

In this publication a camera model was presented which allows to calculate diffuse horizontal irradiance (DHI) and diffuse sky irradiance  $D_i$  in any inclined plane from the RGB image of an all-sky imager (ASI) and global horizontal irradiance (GHI) measured by a pyranometer. The combination of GHI, DHI and  $D_i$  from these sources can then be used to derive direct normal irradiance (DNI) and global tilted irradiance (GTI) in any plane of interest. The proposed method benefits from corrections of the measurands (DHI,  $D_i$ , GTI) based on information available from the ASI firmware and from the comparison of ASI-based DHI and GHI from pyranometer. Two additional corrections treat glare and image saturation, as both influences affect the ASI image in conditions with direct irradiance.

The ASI-based measurement system was developed by DLR at CIEMAT's Plataforma Solar de Almería (PSA) in southern Spain and was validated at PSA and University of Oldenburg in northwestern Germany. At both sites together, the study included approximately 1.5 years of data. The method and applied corrections were developed with the target to reproduce reference DHI from a shaded pyranometer. For DHI and at 1 min resolution, RMSD and BIAS ranged below 18 W/m<sup>2</sup> and  $\pm 5$  W/m<sup>2</sup> for any of the datasets. However, not only DHI was validated. Also the ASI-based prediction of GTI in a variety of planes was benchmarked over state-of-the-art approaches. ASI-based

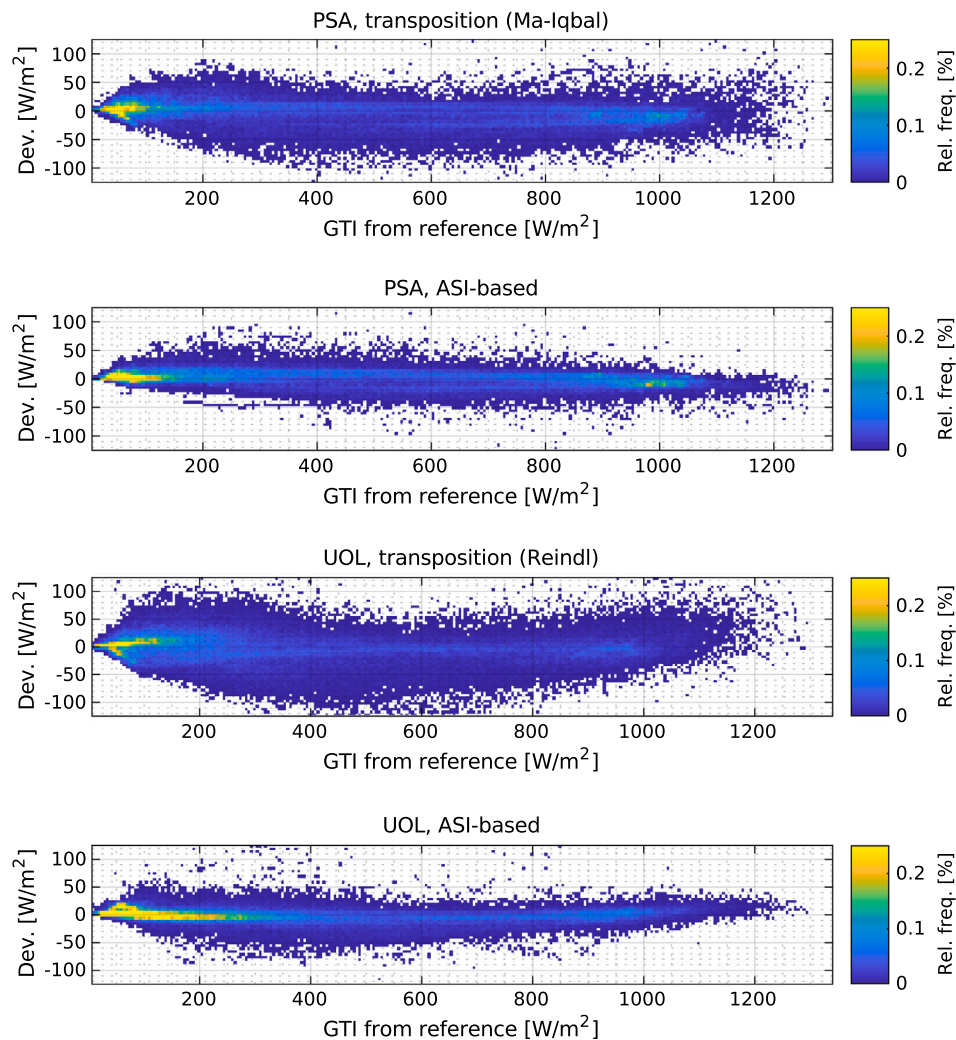


Fig. A.12. Relative frequency of the observed deviation (Dev.) between modeled and reference GTI over reference GTI in a plane with tilt  $45^\circ$ , orientation southwest, temporal resolution of 1 min-average: transposition model Ma-Iqbal (Demain et al., 2013) based on DNI, DHI from solar tracker at CIEMAT's PSA (top), ASI + pyranometer at CIEMAT's PSA (second row), transposition model Reindl (Yang, 2016) based on DNI, DHI from solar tracker at UOL (third row), ASI + pyranometer at UOL (bottom).

prediction of GTI clearly outperformed transposition based on DNI and DHI measured by pyrheliometer and shaded pyranometer in terms of rRMSD. Unsurprisingly, the advantage of the ASI-based measurement was even more pronounced in comparison to modeled GTI based on GHI alone, relying on decomposition and consecutive transposition. Likewise, the proposed method's advantage was found to be more distinct for more inclined planes. rRMSD of the ASI-based measurement of GTI range from 1.6% to 4.8% depending on the evaluated site and tilt of the sensor plane ( $20^\circ \dots 61^\circ$ ), evaluating 10 min sliding averages. rBIAS of the ASI-based GTI measurement range below 1% for all planes which is below the calibration uncertainties of the involved pyranometers. In part, deviations might also be connected to unknown ground albedo and further pyranometer measurement errors, such as cosine errors.

The ASI-based approach in this work also used a thermopile pyranometer. This combination is the basis for the observed high accuracy compared to other approaches that either only use an ASI or only radiometers. We tested the method with two types of surveillance cameras from the same manufacturer. The proposed corrections were parameterized for the validation site and the local hardware in the sense of a self-calibration, only relying on readings from ASI and GHI pyranometer. A separate radiometric calibration of the all-sky imager is avoided. The self-calibration can in principle also be applied to other camera types. It can further be automated in the sense of an online

recalibration which would account for a possible degradation of the camera hardware immediately. Compared to alternative measurements, the hardware is cheap, robust, readily available, avoids moving parts, and allows for further analyses and an application in ASI-based forecasting. The application of the method for other cameras must be tested, but we expect that it can be transferred and adapted to other cameras.

In the present study, we benchmarked ASI-based measurement of GTI over transposition based on DNI and DHI from a high-quality tracker setup and found a substantial advantage. Based on this, we are confident to outperform prediction of GTI based on transposition and DNI, DHI from more economical hardware such as rotating shadow-band irradiometer (RSI), *SPN1 sunshine pyranometer*, *sunshine duration sensor* or *sunto CaptPro* even more clearly.

The method studied here is seen as highly promising. From our study, we expect that a further gain in accuracy and transferability can be achieved by a refined treatment of deviations occurring in the sun's vicinity. To this end, an adapted exposure control has been tested in the meantime, to support the method by images with increased dynamic range. Regarding glare effects, we see empiric corrections based on image features as most promising. More specifically, DHI for which abundant data is available can be used as target to train convolutional neural networks for the glare correction. Finally, the influence of clouds, air mass and aerosols on the spectrum of incident irradiance and

consequently on the measurement will be characterized in the future to apply an optimal broadband correction in each situation.

### Declaration of competing interest

The authors declare that they have no known competing financial interests or personal relationships that could have appeared to influence the work reported in this paper.

### Acknowledgment

This research received funding from the European Union's Horizon 2020 research and innovation programme under grant agreement No 864337 (Smart4RES project).

### Appendix. Scatter-density plots of deviations over influences

Scatter-density plots which were shown in the main part of the publication are reproduced here in a modified version. Figs. A.10–A.12 show the relative frequency of the deviation between model and reference over main influences on the models' performance. These plots may provide additional insight on the models' performance depending on the present atmospheric conditions.

### References

- Alonso-Montesinos, J., Batlles, F., 2015. The use of a sky camera for solar radiation estimation based on digital image processing. *Energy* 90, 377–386. <http://dx.doi.org/10.1016/j.energy.2015.07.028>.
- ASTM, 2020. G 173-03. Standard Tables for Reference Solar Spectral Irradiances: Direct Normal and Hemispherical on 37° Tilted Surface. Standard, ASTM International, West Conshohocken, PA, <http://dx.doi.org/10.1520/G0173-03R20>.
- Chauvin, R., Nou, J., Thil, S., Grieu, S., 2015. Modelling the clear-sky intensity distribution using a sky imager. *Sol. Energy* 119, 1–17. <http://dx.doi.org/10.1016/j.solener.2015.06.026>.
- Clarke, J.A., Cockroft, J., Conner, S., Hand, J.W., Kelly, N.J., Moore, R., O'Brien, T., Strachan, P., 2002. Simulation-assisted control in building energy management systems. *Energy Build.* 34 (9), 933–940. [http://dx.doi.org/10.1016/S0378-7788\(02\)00068-3](http://dx.doi.org/10.1016/S0378-7788(02)00068-3).
- Demain, C., Journée, M., Bertrand, C., 2013. Evaluation of different models to estimate the global solar radiation on inclined surfaces. *Renew. Energy* 50, 710–721. <http://dx.doi.org/10.1016/j.renene.2012.07.031>.
- Dev, S., Savoy, F.M., Lee, Y.H., Winkler, S., 2014. WAHRIS: A low-cost high-resolution whole sky imager with near-infrared capabilities. In: Proceedings of the SPIE/Infrared Imaging Systems: Design, Analysis, Modeling, and Testing XXV. Baltimore, Maryland, United States, 5–9 May 2014. p. 90711L. <http://dx.doi.org/10.1117/12.2052982>.
- Dev, S., Savoy, F.M., Lee, Y.H., Winkler, S., 2019. Estimating solar irradiance using sky imagers. *Atmos. Meas. Tech.* 12 (10), 5417–5429. <http://dx.doi.org/10.5194/amt-12-5417-2019>.
- Dubovik, O., King, M.D., 2000. A flexible inversion algorithm for retrieval of aerosol optical properties from Sun and sky radiance measurements. *J. Geophys. Res.: Atmos.* 105 (D16), 20673–20696. <http://dx.doi.org/10.1029/2000JD900282>.
- Elminir, H.K., Benda, V., Tousek, J., 2001. Effects of solar irradiation conditions and other factors on the outdoor performance of photovoltaic modules. *J. Electr. Eng.* 52 (5/6), 125–133.
- Fabel, Y., Nouri, B., Wilbert, S., Blum, N., Triebel, R., Hasenbalg, M., Kuhn, P., Zarzalejo, L.F., Pitz-Paal, R., 2021. Applying self-supervised learning for semantic cloud segmentation of all-sky images. *Atmos. Meas. Tech. Discuss.* 2021, 1–20. <http://dx.doi.org/10.5194/amt-2021-1>.
- Gauchet, C., Blanc, P., Espinar, B., Charbonnier, B., Demengel, D., 2012. Surface solar irradiance estimation with low-cost fish-eye camera. In: Workshop on "Remote Sensing Measurements for Renewable Energy". Risoe, Denmark, 22–23 May 2012. URL: <https://hal-mines-paristech.archives-ouvertes.fr/hal-00741620>.
- Geuder, N., Quaschnig, V., 2006. Soiling of irradiation sensors and methods for soiling correction. *Sol. Energy* 80 (11), 1402–1409. <http://dx.doi.org/10.1016/j.solener.2006.06.001>.
- Geuder, N., Wolfertstetter, F., Wilbert, S., Schüler, D., Affolter, R., Kraas, B., Lüpfer, E., Espinar, B., 2015. Screening and flagging of solar irradiation and ancillary meteorological data. *Energy Procedia* 69, 1989–1998. <http://dx.doi.org/10.1016/j.egypro.2015.03.205>.
- Grossberg, M.D., Nayar, S.K., 2002. What can be known about the radiometric response from images? In: Computer Vision — ECCV 2002 Proceedings, Part IV/ 7th European Conference on Computer Vision. Copenhagen, Denmark, 28–31 May 2002. pp. 189–205. [http://dx.doi.org/10.1007/3-540-47979-1\\_13](http://dx.doi.org/10.1007/3-540-47979-1_13).
- Gueymard, C.A., 2001. Parameterized transmittance model for direct beam and circumsolar spectral irradiance. *Sol. Energy* 71 (5), 325–346. [http://dx.doi.org/10.1016/S0038-092X\(01\)00054-8](http://dx.doi.org/10.1016/S0038-092X(01)00054-8).
- Gueymard, C.A., 2005. SMARTS Code, Version 2.9.5: Users Manual. Technical Report, Solar Consulting Services, URL: [https://www.solarconsultingservices.com/SMARTS295\\_Users\\_Manual\\_PC.pdf](https://www.solarconsultingservices.com/SMARTS295_Users_Manual_PC.pdf).
- Gueymard, C.A., 2009. Direct and indirect uncertainties in the prediction of tilted irradiance for solar engineering applications. *Sol. Energy* 83 (3), 432–444. <http://dx.doi.org/10.1016/j.solener.2008.11.004>.
- Gueymard, C.A., Ivanova, S., 2018. Progress in sky radiance and luminance modeling using circumsolar radiation and sky view factors. In: Proceedings of 12th International Conference on Solar Energy for Buildings and Industry/ EuroSun 2018. Rapperswil, Switzerland, 10–13 September 2018. <http://dx.doi.org/10.18086/eurosun2018.09.16>.
- Inanici, M., 2010. Evaluation of high dynamic range image-based sky models in lighting simulation. *Leukos* 7 (2), 69–84. <http://dx.doi.org/10.1582/LEUKOS.2010.07.02001>.
- Ineichen, P., 2007. Sky Luminance/Radiance Distribution Quality Control. Technical Report, EC, Geneva, URL: <https://archive-ouverte.unige.ch/unige:23638>.
- Ineichen, P., 2008. Comparison and validation of three global-to-beam irradiance models against ground measurements. *Sol. Energy* 82 (6), 501–512. <http://dx.doi.org/10.1016/j.solener.2007.12.006>.
- Ineichen, P., Perez, R., 2002. A new airmass independent formulation for the Linke turbidity coefficient. *Sol. Energy* 73 (3), 151–157. [http://dx.doi.org/10.1016/S0038-092X\(02\)00045-2](http://dx.doi.org/10.1016/S0038-092X(02)00045-2).
- International Electrotechnical Commission, 1999. Multimedia systems and equipment – Colour measurement and management – Part 2-1: Colour management – Default RGB colour space - sRGB. IEC 61966-2-1:1999. Geneva, Switzerland.
- International Electrotechnical Commission, 2015. Photovoltaic System Performance – Part 1: Monitoring. IEC 61724-1. Geneva, Switzerland.
- International Organization for Standardization, 1993. Solar energy – Calibration of a pyranometer using a pyrheliometer. ISO 9846:1993. Geneva, Switzerland.
- International Organization for Standardization, 2018. Solar energy – specification and classification of instruments for measuring hemispherical solar and direct solar radiation. ISO 9060:2018. Geneva, Switzerland.
- Kazantzidis, A., Tzoumanikas, P., Nikitidou, E., Salamalikis, V., Wilbert, S., Prah, C., 2017. Application of simple all-sky imagers for the estimation of aerosol optical depth. *AIP Conf. Proc.* 1850 (1), 140012. <http://dx.doi.org/10.1063/1.4984520>.
- Kim, K.H., Oh, J.K.-W., Jeong, W., 2016. Study on solar radiation models in South Korea for improving office building energy performance analysis. *Sustainability* 8 (6), 589. <http://dx.doi.org/10.3390/su8060589>.
- Kottek, M., Grieser, J., Beck, C., Rudolf, B., Rubel, F., 2006. World map of the Köppen-Geiger climate classification updated. *Meteorol. Z.* 15 (3), 259–263. <http://dx.doi.org/10.1127/0941-2948/2006/0130>.
- Kuhn, P., Wilbert, S., Prah, C., Schüler, D., Haase, T., Hirsch, T., Wittmann, M., Ramirez, L., Zarzalejo, L., Meyer, A., Vuilleumier, L., Blanc, P., Pitz-Paal, R., 2017. Shadow camera system for the generation of solar irradiance maps. *Sol. Energy* 157, 157–170. <http://dx.doi.org/10.1016/j.solener.2017.05.074>.
- Kurtz, B., Kleissl, J., 2017. Measuring diffuse, direct, and global irradiance using a sky imager. *Sol. Energy* 141, 311–322. <http://dx.doi.org/10.1016/j.solener.2016.11.032>.
- Lave, M., Hayes, W., Pohl, A., Hansen, C.W., 2015. Evaluation of global horizontal irradiance to plane-of-array irradiance models at locations across the United States. *IEEE J. Photovolt.* 5 (2), 597–606. <http://dx.doi.org/10.1109/JPHOTOV.2015.2392938>.
- Lazos, D., Sproul, A.B., Kay, M., 2014. Optimisation of energy management in commercial buildings with weather forecasting inputs: A review. *Renew. Sustain. Energy Rev.* 39, 587–603. <http://dx.doi.org/10.1016/j.rser.2014.07.053>.
- Lee, Jr., R.L., Devan, D.E., 2008. Observed brightness distributions in overcast skies. *Appl. Opt.* 47 (34), H116–H127. <http://dx.doi.org/10.1364/AO.47.00H116>.
- Li, D.H., Lam, J.C., 2004. Predicting solar irradiance on inclined surfaces using sky radiance data. *Energy Convers. Manage.* 45 (11–12), 1771–1783. <http://dx.doi.org/10.1016/j.enconman.2003.09.020>.
- Loutzenhiser, P.G., Manz, H., Felsmann, C., Strachan, P.A., Frank, T., Maxwell, G.M., 2007. Empirical validation of models to compute solar irradiance on inclined surfaces for building energy simulation. *Sol. Energy* 81 (2), 254–267. <http://dx.doi.org/10.1016/j.solener.2006.03.009>.
- Mejia, F.A., Kurtz, B., Murray, K., Hinkelmann, L.M., Sengupta, M., Xie, Y., Kleissl, J., 2016. Coupling sky images with radiative transfer models: a new method to estimate cloud optical depth. *Atmos. Meas. Tech.* 9 (8), 4151–4165. <http://dx.doi.org/10.5194/amt-9-4151-2016>.
- Mungra, M., Li, Y., Pravattoni, M., Lennon, A., 2021. Impact of angular irradiation profiles on performance of silicon PV modules using light scattering films. *IEEE J. Photovolt.* 11, 750–759. <http://dx.doi.org/10.1109/JPHOTOV.2020.3048893>.
- Nann, S., Riordan, C., 1991. Solar spectral irradiance under clear and cloudy skies: Measurements and a semiempirical model. *J. Appl. Meteorol.* 30 (4), 447–462. [http://dx.doi.org/10.1175/1520-0450\(1991\)030<0447:SSIUCA>2.0.CO;2](http://dx.doi.org/10.1175/1520-0450(1991)030<0447:SSIUCA>2.0.CO;2).

- Nouri, B., Wilbert, S., Blum, N., Kuhn, P., Schmidt, T., Yasser, Z., Schmidt, T., Zarzalejo, L.F., Lopes, F.M., Silva, H.G., Schroedter-Homscheidt, M., Kazantzidis, A., Raeder, C., Blanc, P., Pitz-Paal, R., 2020. Evaluation of an all sky imager based nowcasting system for distinct conditions and five sites. *AIP Conf. Proc.* 2303 (1), 180006. <http://dx.doi.org/10.1063/5.0028670>.
- Reinhart, C.F., Walkenhorst, O., 2001. Validation of dynamic RADIANCE-based daylight simulations for a test office with external blinds. *Energy Build.* 33 (7), 683–697. [http://dx.doi.org/10.1016/S0378-7788\(01\)00058-5](http://dx.doi.org/10.1016/S0378-7788(01)00058-5).
- Riechelmann, S., Schrempf, M., Seckmeyer, G., 2013. Simultaneous measurement of spectral sky radiance by a non-scanning multidirectional spectroradiometer (MUDIS). *Meas. Sci. Technol.* 24 (12), 125501. <http://dx.doi.org/10.1088/0957-0233/24/12/125501>.
- Román, R., Antón, M., Cazorla, A., de Miguel, A., Olmo, F.J., Bilbao, J., Alados-Arboledas, L., 2012. Calibration of an all-sky camera for obtaining sky radiance at three wavelengths. *Atmos. Meas. Tech.* 5 (8), 2013–2024. <http://dx.doi.org/10.5194/amt-5-2013-2012>.
- Rossini, E.G., Krenzinger, A., 2007. Maps of sky relative radiance and luminance distributions acquired with a monochromatic CCD camera. *Sol. Energy* 81 (11), 1323–1332. <http://dx.doi.org/10.1016/j.solener.2007.06.013>.
- Scaramuzza, D., Martinelli, A., Siegwart, R., 2006. A toolbox for easily calibrating omnidirectional cameras. In: 2006 IEEE/RSJ International Conference on Intelligent Robots and Systems. Beijing, China, 9–15 October 2006. pp. 5695–5701. <http://dx.doi.org/10.1109/IROS.2006.282372>.
- Schmidt, T., Kalisch, J., Lorenz, E., Heineman, D., 2015. Retrieving direct and diffuse radiation with the use of sky imager pictures. In: EGU General Assembly Conference Abstracts. Vienna, Austria, 12–17 April 2015.
- Sengupta, M., Habte, A., Gueymard, C., Wilbert, S., Renné, D., Blanc, P., Dobos, A., et al., 2017. Best Practices Handbook for the Collection and Use of Solar Resource Data for Solar Energy Applications: Second Edition. Technical Report. United States. <http://dx.doi.org/10.2172/1411856>.
- Shields, J.E., Karr, M.E., Tooman, T.P., Sowle, D.H., Moore, S.T., 1998. The whole sky imager—a year of progress. In: Eighth Atmospheric Radiation Measurement (ARM) Science Team Meeting. Tucson, Arizona, March 1998. pp. 23–27. URL: [https://www.researchgate.net/publication/243774417\\_The\\_Whole\\_Sky\\_Imager\\_-\\_A\\_Year\\_of\\_Progress](https://www.researchgate.net/publication/243774417_The_Whole_Sky_Imager_-_A_Year_of_Progress).
- Siddiqui, T.A., Bharadwaj, S., Kalyanaraman, S., 2019. A deep learning approach to solar-irradiance forecasting in sky-videos. In: 2019 IEEE Winter Conference on Applications of Computer Vision (WACV). Waikoloa, HI, USA, 7–11 January 2019. pp. 2166–2174. <http://dx.doi.org/10.1109/WACV.2019.00234>.
- sunto, 2018. All-Out Irradiation Sensor. Data Sheet V1.0, URL: [https://www.sunto-technology/wp-content/uploads/2019/05/CaptPro\\_EU-Datasheet.pdf](https://www.sunto-technology/wp-content/uploads/2019/05/CaptPro_EU-Datasheet.pdf).
- Tohsing, K., Schrempf, M., Riechelmann, S., Schilke, H., Seckmeyer, G., 2013. Measuring high-resolution sky luminance distributions with a CCD camera. *Appl. Opt.* 52 (8), 1564–1573. <http://dx.doi.org/10.1364/AO.52.001564>.
- Toledo, C., Gracia Amillo, A.M., Bardizza, G., Abad, J., Urbina, A., 2020. Evaluation of solar radiation transposition models for passive energy management and building integrated photovoltaics. *Energies* 13 (3), 702. <http://dx.doi.org/10.3390/en13030702>.
- Voss, K.J., Zibordi, G., 1989. Radiometric and geometric calibration of a visible spectral electro-optic “fish-eye” camera radiance distribution system. *J. Atmos. Ocean. Technol.* 6 (4), 652–662. [http://dx.doi.org/10.1175/1520-0426\(1989\)006<0652:Ragcoa>2.0.Co;2](http://dx.doi.org/10.1175/1520-0426(1989)006<0652:Ragcoa>2.0.Co;2).
- Vuilleumier, L., Félix, C., Vignola, F., Blanc, P., Badosa, J., Kazantzidis, A., Calpini, B., 2017. Performance evaluation of radiation sensors for the solar energy sector. *Meteorol. Z.* 26 (5), 485–505. <http://dx.doi.org/10.1127/metz/2017/0836>.
- Vuilleumier, L., Hauser, M., Félix, C., Vignola, F., Blanc, P., Kazantzidis, A., Calpini, B., 2014. Accuracy of ground surface broadband shortwave radiation monitoring. *J. Geophys. Res.: Atmos.* 119 (24), 13838–13860. <http://dx.doi.org/10.1002/2014JD022335>.
- Wacker, S., Gröbner, J., Zysset, C., Diener, L., Tzoumanikas, P., Kazantzidis, A., Vuilleumier, L., Stöckli, R., Nyeki, S., Kämpfer, N., 2015. Cloud observations in Switzerland using hemispherical sky cameras. *J. Geophys. Res.: Atmos.* 120 (2), 695–707. <http://dx.doi.org/10.1002/2014jd022643>.
- West, S.R., Rowe, D., Sayeef, S., Berry, A., 2014. Short-term irradiance forecasting using skycams: Motivation and development. *Sol. Energy* 110, 188–207. <http://dx.doi.org/10.1016/j.solener.2014.08.038>.
- Westbrook, O.W., 2015. A sky radiance-based approach to diffuse irradiance transposition. In: 2015 IEEE 42nd Photovoltaic Specialist Conference (PVSC). New Orleans, LA, USA 14–19 June 2015. pp. 1–5. <http://dx.doi.org/10.1109/PVSC.2015.7356210>.
- Wilbert, S., Kleindiek, S., Nouri, B., Geuder, N., Habte, A., Schwandt, M., Vignola, F., 2016. Uncertainty of rotating shadowband irradiometers and si-pyranometers including the spectral irradiance error. *AIP Conf. Proc.* 1734 (1), 150009. <http://dx.doi.org/10.1063/1.4949241>.
- Yang, D., 2016. Solar radiation on inclined surfaces: Corrections and benchmarks. *Sol. Energy* 136, 288–302. <http://dx.doi.org/10.1016/j.solener.2016.06.062>.